A REAL-TIME 3D SCANNER SYSTEM DEVELOPED WITH COMBINED USAGE OF ACTIVE TRIANGULATION AND TIME OF FLIGHT SENSORS

A Thesis Submitted to
The Graduate School of
İzmir Institute of Technology
in Partial Fulfillment of the Requirements for the Degree of

MASTER OF SCIENCE

in Electronics and Communication Engineering

by

Burak ŞİMŞEK

July 2023

İZMİR

ACKNOWLEDGMENTS

I would like to express my deepest gratitude to my supervisor, Assoc. Prof. Dr. Şevket GÜMÜŞTEKİN, for his invaluable guidance, unwavering support, and continuous encouragement throughout the entire process of this thesis. His expertise, insightful feedback, and patience have been instrumental in shaping the direction of my research and improving the quality of this work.

I am also grateful to İsmail Hancı, the manager of Teknodef Defence Systems Company, for his exceptional support and assistance during this thesis. His visionary leadership, mentorship, and dedication to academic excellence have been truly inspiring. His valuable insights and suggestions have significantly enriched my understanding of the subject matter.

I would like to extend my appreciation to the members of my thesis committee, Asst. Prof. Dr. Abdurrahman GÜMÜŞ and Asst. Prof. Dr. Başak Esin GÜZEL, for their valuable insights, constructive criticism, and suggestions that have greatly contributed to the refinement of this thesis.

My sincere thanks go to my colleagues and friends for their support, discussions, and encouragement throughout this journey. Their friendship and camaraderie have made the process more enjoyable and inspiring.

Lastly, I am deeply grateful to my family and especially to my spouse, Kübra, for their unconditional love, unwavering belief in my abilities, and constant motivation. Their encouragement and sacrifices have been the driving force behind my academic achievements.

In conclusion, I am indebted to all those who have contributed to the completion of this thesis. Your support and encouragement have played a crucial role in my academic growth and success.

We approve the thesis of **Burak ŞİMŞEK**

Examining Committee Members:

Assoc. Prof. Dr. Şevket Gümüştekin
Department of Electrical and Electronics Engineering, Izmir Institute of Technology

Asst. Prof. Dr. Abdurrahman Gümüş
Department of Electrical and Electronics Engineering, Izmir Institute of Technology

Asst. Prof. Dr. Başak Esin Güzel
Department of Electrical and Electronics Engineering, Izmir Democracy University

19 July 2023

Assoc. Prof. Dr. Şevket Gümüştekin
Supervisor, Department of Electrical and
Electronics Engineering
Izmir Institute of Technology

Prof. Dr. Mustafa Aziz ALTINKAYA
Head of the Department of
Electrical and Electronics Engineering

Prof. Dr. Mehtap EANES
Dean of the Graduate School of
Engineering and Science

ABSTRACT

A REAL-TIME 3D SCANNER SYSTEM DEVELOPED WITH COMBINED USAGE OF ACTIVE TRIANGULATION AND TIME OF FLIGHT SENSORS

This study presents the development and evaluation of a real-time 3D scanner system that combines active triangulation and time of flight sensor technologies. The aim of this research is to design a robust and efficient system capable of capturing accurate 3D models of objects.

The proposed system utilizes active triangulation, which involves projecting structured light patterns onto the target and capturing the reflected patterns using a camera. Additionally, a time of flight (TOF) sensor is incorporated to measure the time it takes for light to travel to the target and back, enabling depth information to be obtained.

The implementation of the system involves the integration of hardware components, calibration procedures, and software algorithms. The hardware setup includes a high-resolution camera, laser projectors, and a TOF sensor. Calibration techniques are employed to establish accurate correspondence between the camera, projectors, and the TOF sensor. Various computational algorithms, such as point cloud registration and surface reconstruction, are employed to process the acquired data and generate a complete 3D model.

The performance evaluation of the developed system includes tests on different objects and scenes with varying levels of complexity. The results demonstrate the system's ability to capture detailed 3D models in real-time, with high accuracy and resolution. The system proves to be robust against environmental factors such as ambient lighting and object reflectivity.

The findings of this study contribute to the field of 3D scanning by presenting a practical and efficient approach for real-time 3D model acquisition. The developed system has potential applications in any field of research and industry that can utilize fast and accurate 3D scanning.

ÖZET

AKTİF ÜÇGENLEME VE VARIŞ ZAMANI SENSÖRLERİNİN BİRLİKTE KULLANIMIYLA GELİŞTİRİLEN GERÇEK ZAMANLI BİR 3B TARAYICI SİSTEMİ

Bu çalışma, aktif üçgenleme ve uçuş zamanı sensörü teknolojilerini birleştiren gerçek zamanlı bir 3 boyutlu tarayıcı sisteminin geliştirilmesini ve değerlendirilmesini sunmaktadır. Bu araştırmanın amacı, nesnelerin hassas 3 boyutlu modellerini yakalayabilen sağlam ve verimli bir sistem tasarlamaktır.

Önerilen sistem, yapılandırılmış ışık desenlerinin hedefe yansıtılmasını ve yansıyan desenlerin bir kamera kullanılarak yakalanmasını içeren aktif üçgenlemeyi kullanır. Ek olarak, ışığın hedefe gidip geri gitmesi için geçen süreyi ölçen bir uçuş süresi (TOF) sensörü dahil edilerek derinlik bilgisinin elde edilmesi sağlanır.

Sistemin uygulanması donanım bileşenlerinin, kalibrasyon prosedürlerinin ve yazılım algoritmalarının entegrasyonunu içerir. Donanım kurulumunda yüksek çözünürlüklü bir kamera, lazer projektörler ve bir TOF sensörü bulunur. Kamera, projektör ve TOF sensörü arasında doğru eşleşmeyi sağlamak için kalibrasyon teknikleri kullanılır. Elde edilen verileri işlemek ve tam bir 3 boyutlu model oluşturmak için nokta bulutu kaydı ve yüzey yeniden yapılandırması gibi çeşitli hesaplama algoritmaları kullanılır.

Geliştirilen sistemin performans değerlendirmesi, farklı karmaşıklık düzeylerine sahip farklı nesneler üzerinde yapılan testleri içermektedir. Sonuçlar, sistemin ayrıntılı 3D modelleri gerçek zamanlı olarak yüksek doğruluk ve çözünürlükle yakalama yeteneğini göstermektedir. Sistemin ortam aydınlatması ve nesne yansıması gibi çevresel faktörlere karşı dayanıklı olduğu görülmektedir.

Bu çalışmanın bulguları, gerçek zamanlı 3 boyutlu model edinimi için pratik ve etkili bir yaklaşım sunarak 3 boyutlu tarama alanına katkı sağlamaktadır. Geliştirilen sistemin hızlı ve hassas 3B tarama işleminden faydalabilecek tüm araştırma ve endüstri alanlarında uygulanma potansiyeli vardır.

TABLE OF CONTENTS

LIST OF FIGURES

LIST OF SYMBOLS

O_C	Camera center
O_L	Laser diode center
$d\alpha$	Half the angle of the camera field of view
t	Distance between any pixel where the laser is detected and the camera center
k	Angle between the reflection axes of the laser and camera
p	Distance between any pixel where the laser reflects and the laser diode
d	Distance between camera sensor and laser diode
θ	Angle between camera and laser principal axis
$o_{x,y}$	Pixel coordinate of the image center (principal points)
f_c	Focal length
$s_{x,y}$	effective size of pixel (horizontal and vertical direction)
sz_{px}	Size of pixel
u	Vertical distance of the any pixel where the laser reflects from the optical center
v	Horizontal distance of the any pixel where the laser reflects from the optical center
X	Distance of X axis
Y	Distance of Y axis
Z	Distance of X axis (Depth)
γ	Resolution angle
R	Radius
a	Screw thread pitch
n	Number of turns

LIST OF ABBREVIATIONS

3D	Three Dimension
ToF	Time of Flight
CCD	Charged Coupled Device
CAM	Computer-Aided Manufacturing
PWM	Pulse Width Modulation
IP	Internet Protocol
TTL	Transistor-Transistor Logic
USB	Universal Serial Bus
HD	High-Definition
CMOS	Complementary Metal-Oxide Semiconductor
ARM	Advanced RISC Machine
ADC	Analog Digital Converter
IO	Input-Output
DC	Direct Current
MCU	Microcontroller Unit
RGB	Red-Green-Blue
NMA	Nelder–Mead method
CW	Clockwise
CCW	Counterclockwise
LASER	Light Amplification by Stimulated Emission of Radiation

CHAPTER 1

INTRODUCTION

1.1. Overview of 3D Reconstruction System

The rapid progress in computer vision has significantly impacted various industries, such as robotics, entertainment, medicine, and architecture. Among the many areas within this field, one that stands out is 3D reconstruction, which seamlessly combines the physical and digital domains. Essentially, 3D reconstruction involves capturing real-world objects and scenes in three dimensions, offering a wide range of applications that continuously evolve and redefine how we visually represent things.

The pursuit of 3D reconstruction is essentially an attempt to mimic human-like perception of objects and scenes in their spatial context. This complex endeavor relies on a delicate interplay of computational techniques, image processing algorithms, and mathematical models. The primary goal is to recreate the shape, structure, and appearance of objects using only 2D images or sensor data. The significance of this process goes beyond enhancing the realism of virtual environments; it has the potential to revolutionize practical applications in various fields (Ham, et al., 2019).

For instance, consider the field of archaeology (Figure 1), where 3D reconstruction plays a crucial role in digitally preserving ancient artifacts and monuments. By meticulously reconstructing these items in a 3D space, researchers and enthusiasts gain unprecedented opportunities for virtual exploration, preservation, and education. In the medical field (Figure 2), the precision of 3D models assists surgeons in visualizing intricate anatomical details, leading to improved surgical planning and better patient outcomes. The entertainment industry (Figure 3) thrives on the captivating appeal of lifelike character animations and immersive virtual worlds, all made possible by sophisticated 3D reconstruction techniques. Additionally, the safe navigation of complex urban environments (Figure 4) by autonomous vehicles becomes feasible through the utilization of 3D reconstruction technologies (Moncef, et al., 2019).

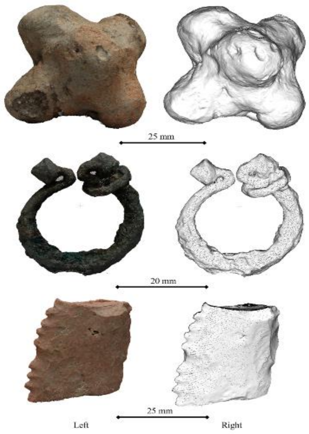

Figure 1. 3D Reconstruction Study for Small Archaeological Remains (Source: (Rodríguez-Martín, et al., 2020))

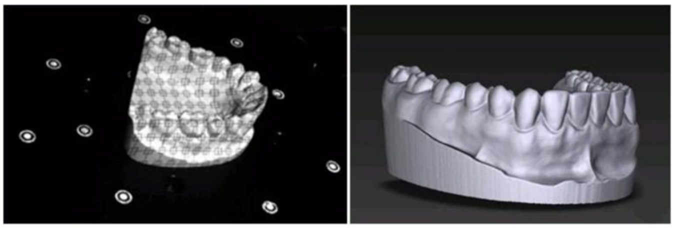

Figure 2. 3D Reconstruction Study for Human Anatomical Structure (Source: (Azevedo and Teresa, 2012))

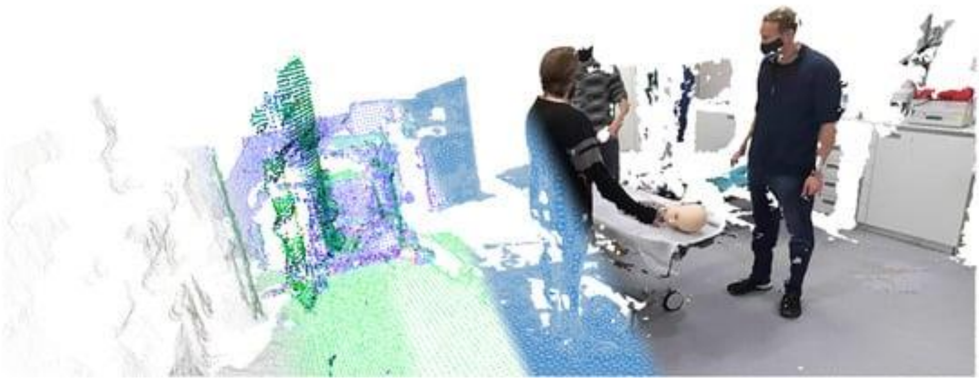

Figure 3. 3D Reconstruction Study for Virtual World (Source: (Eck, et al., 2023))

Figure 4. 3D Reconstruction of Historical Cities (Source: (Pulcrano, et al., 2019))

However, achieving successful 3D reconstruction comes with its own set of challenges that require innovative solutions. Factors like different lighting conditions, various camera settings, objects blocking the view, and changes in perspective make the reconstruction process complex. Moreover, dealing with different types of data sources, from regular photos to complex depth maps and point clouds, demands advanced algorithms to blend these different inputs into a coherent 3D representation.

Researchers have tackled these challenges using various methods tailored to specific situations and goals. For example, photogrammetry extracts detailed depth information from multiple images, allowing for highly accurate 3D models. On the other hand, laser scanning uses precise laser measurements to capture distances and create detailed point clouds, leading to highly detailed reconstructions. Recent advancements in deep learning have opened up new possibilities, enabling neural networks to understand the complex connections between 2D images and their corresponding 3D structures.

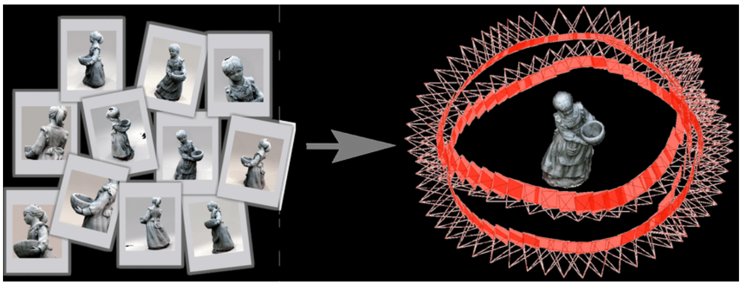

Figure 5. 3D reconstruction using Structure from Motion (Source: (Bianco, et al., 2018))

This thesis explores 3D reconstruction, covering its theory, methods, and practical uses.

A thorough discussion is presented on 3D reconstruction. To understand the basic concept of how images are created, what point clouds are, and how ordinary 2D pictures become detailed 3D models. We also refer to, methods, algorithms, and real-world examples, providing a snapshot of the current state of 3D reconstruction.

1.1.1. 3D Reconstruction using Structured Lighting

In the evolving fields of computer vision and visual perception, the transformation of two-dimensional images into intricate, lifelike three-dimensional representations holds far-reaching implications across disciplines. At the forefront of this pursuit lies "3D Reconstruction Using Structured Lighting." This technique employs carefully designed light patterns to reveal data from the third dimension, translating 2D images into detailed 3D models (Jens Guehring, 2000). The integration of structured lighting with advanced computational algorithms has revolutionized the process of reconstruction, thus providing a major contribution to visual understanding.

Structured lighting involves projecting precisely crafted light patterns onto objects or scenes (Figure 6). These patterns introduce controlled variations in how light interacts with surfaces. Analyzing the resulting distortions reveals depth information, unveiling the topography of the object under study.

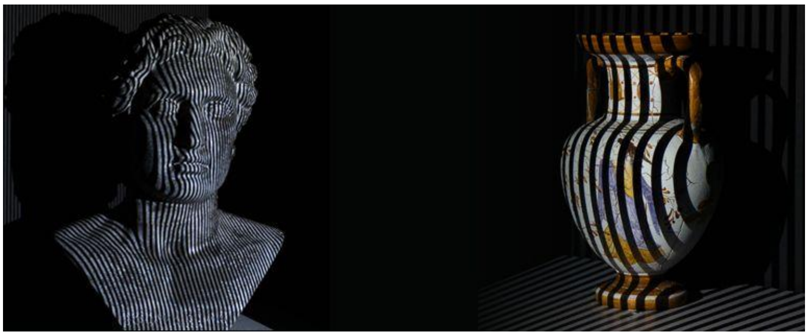

Figure 6. Structured-Light Scanning System (Source: (Gupta, et al., 2011))

Structured lighting is used in diverse applications. In 3D scanning systems for quality control, calibrated projectors emit light patterns onto components, enabling micron-level analysis of deviations from the ideal shape. This technology has transformed inspection processes in industries from automotive manufacturing to aerospace engineering. Progress in structured lighting techniques is fueled by hardware advancements and refined algorithms. High-speed projectors, calibrated cameras, and advanced optics enhance data accuracy. Computational algorithms handle vast data sets, ensuring real-time reconstruction in challenging scenarios like complex shapes and varying lighting.

Challenges include ambient lighting effects and dynamic environments. Addressing these requires hardware design, calibration, and adaptive tracking methods. This thesis explores 3D reconstruction using structured lighting. Through theoretical analysis and practical applications, we unravel its potential across domains. Literature review, experimentation, and analysis illuminate its strengths and limitations.

1.1.1.1. 3D Scanner System using Laser Stripe and Time-of-Flight Sensor

At its core, the "3D Scanner System Using Laser Stripe and Time-of-Flight Sensor" leverages the complementary strengths of laser stripe projection and time-of-flight sensing. Laser stripes, projected onto objects or scenes, interact with surfaces, capturing subtle details through their deformation. Simultaneously, the time-of-flight sensor measures the round-trip travel time of light, providing precise distance information for each point on the object. This dual approach, results in the creation of intricate and lifelike three-dimensional models, rich in detail and accuracy.

This research focuses on the development and evaluation of a real-time 3D scanner system that combines the advantages of active triangulation and time of flight (TOF) sensor technologies. Active triangulation involves projecting structured light patterns onto the target object or scene and capturing the reflected patterns using a camera. This technique allows fast and precise measurements of surface geometry using some image processing. On the other hand, TOF sensors measure the time it takes for light to travel to the target and back, providing depth information based on the speed of light. By integrating these two complementary technologies, the proposed system aims to overcome their individual limitations and deliver a robust and efficient solution for real-time 3D model acquisition. Figures 7, 8 and 9 show examples of laser 3D reconstruction studies.

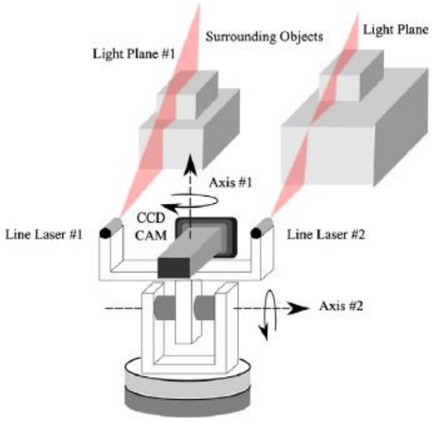

Figure 7. Environment 3D scanner (Source: (Ozan and Gümüştekin, 2013))

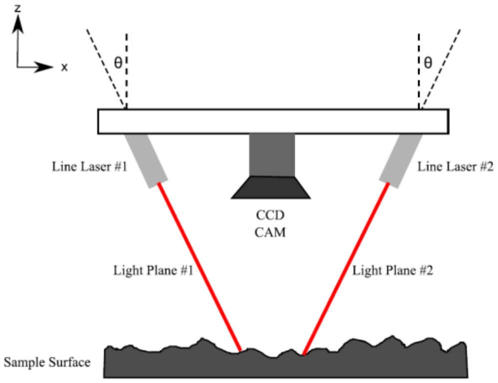

Figure 8. Surface 3D Scanner (Source: (Ozan and Gümüştekin, 2013))

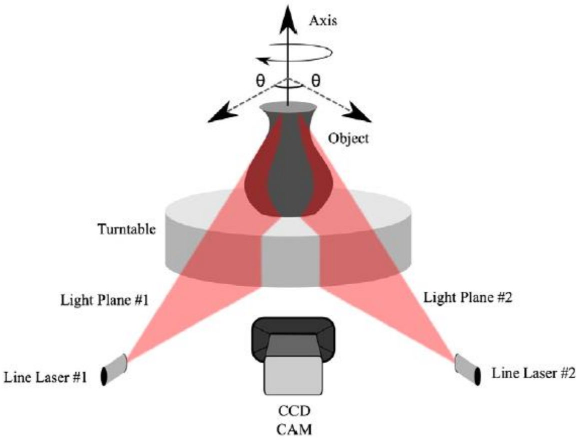

Figure 9. Object 3D Scanner (Source: (Ozan and Gümüştekin, 2013))

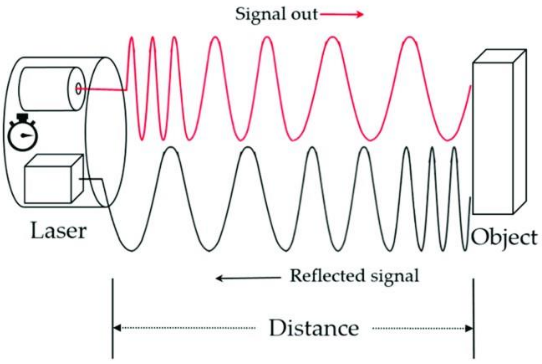

Figure 10. Time of Flight Sensor (ToF) (Source: (Zheng, et al., 2019))

The main objectives of this study encompass the development and integration of hardware components, calibration procedures, and software algorithms. The hardware setup includes a high-resolution camera, a laser projector for structured light projection, and a TOF sensor for depth measurement. Careful calibration techniques are employed to establish accurate correspondences between the camera, projector, and TOF sensor, ensuring precise data acquisition. On the software side, advanced algorithms such as point cloud registration and surface reconstruction are utilized to process the acquired data and generate complete and visually appealing 3D models (Durante, et al., 2017).

A critical aspect of this research is the performance evaluation of the developed system. Extensive tests are conducted on various objects with different complexities to assess the system's accuracy, resolution, and robustness. Factors such as ambient lighting conditions, object reflectivity, and motion are taken into account to evaluate the system's reliability in real-world scenarios. The results of the performance evaluation demonstrate the system's capability to capture highly detailed and accurate 3D models in real-time, showcasing its potential for practical applications.

The findings of this study contribute to the field of 3D scanning by presenting a practical and efficient approach for real-time 3D model acquisition. The developed system has the potential to revolutionize industries such as entertainment, manufacturing, architecture, and archaeology by enabling faster and more accurate data capture. Furthermore, it opens up new avenues for research and development in areas such as virtual reality, augmented reality, and digital preservation.

CHAPTER 2

3D SCANNER SYSTEM WITH TWO LASER AND TOF SENSOR

This chapter will provide detailed information on Mechanical System Design, System Architecture, and System Network Topology.

2.1. Mechanical System Design

The general view of the project mechanism is shown in Figure 11. This device is basically a cart with a movement that allow scanning with line lasers. A ToF sensor is moved in a direction perpendicular to the movement of cart. The first version of this cart was used in (Ozan and Sevket Gumustekin, 2012). This updated version includes an improvement controller board and enhanced hardware components. Main update in this version is the inclusion of the ToF sensor.

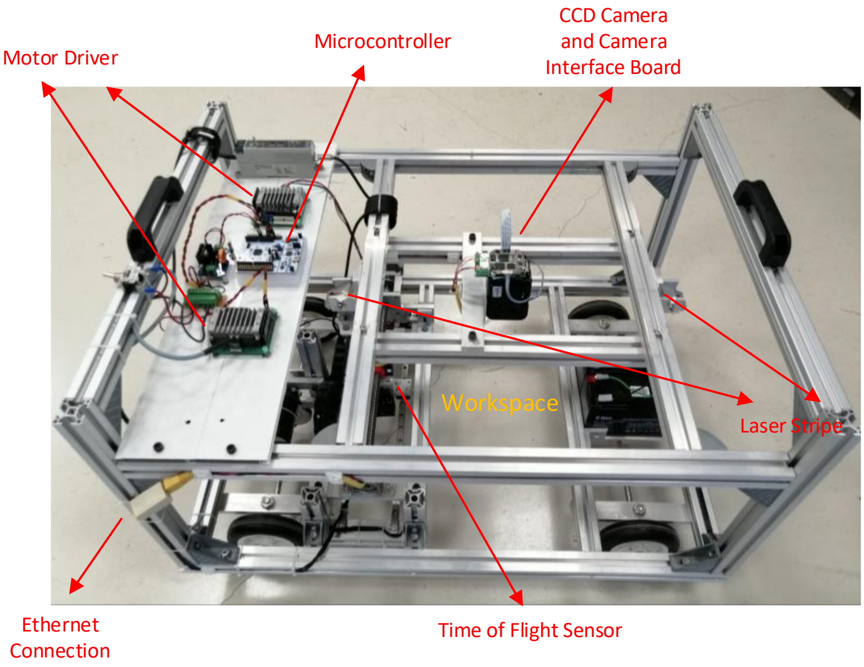

Figure 11. Scanning cart used in the project

The system moves on four wheels and its movement is achieved by driving only two wheels. The step motor that provides the movement is connected to these two wheels with a pulley drive system (Figure 12). The amount of movement of the step motor per step is calculated based on the radius ratios of the two gears in the pulley drive system (Eq. 2.1). When the step motor takes one step, the entire mechanism moves 0.1 mm (Eq. 2.3). Additionally, there is a Time-of-Flight sensor mounted on a separate stepper motor underneath the system. The motion axes of the entire mechanism and the time of flight (ToF) sensor are shown in Figure 12. In order to enhance clarity and provide clearer calculations, the system is also illustrated with symbolic diagrams in Figure 14. The radius of the wheel is denoted as R_1, the radius of the gear connected to the wheel is denoted as R_2, and the radius of the gear connected to the motor is denoted as R_3. The equation representing the relationship between the radii and the displacement of the system is shown as equation 2.1. The value of "n" represents the number of rotations (not step count) for the stepper motors. The step size for the Wheel Hub Motor is 0.36 degrees, and the step size for the Screw Motor is 0.72 degrees. The equations provide the motion distances of the motors in one step. Additionally, the Screw Thread Pitch value is represented as "a". The motion distance of the ToF sensor mounted on the screw is indicated as "y". The relationship between the screw thread pitch and "y" is depicted in equation 2.4.

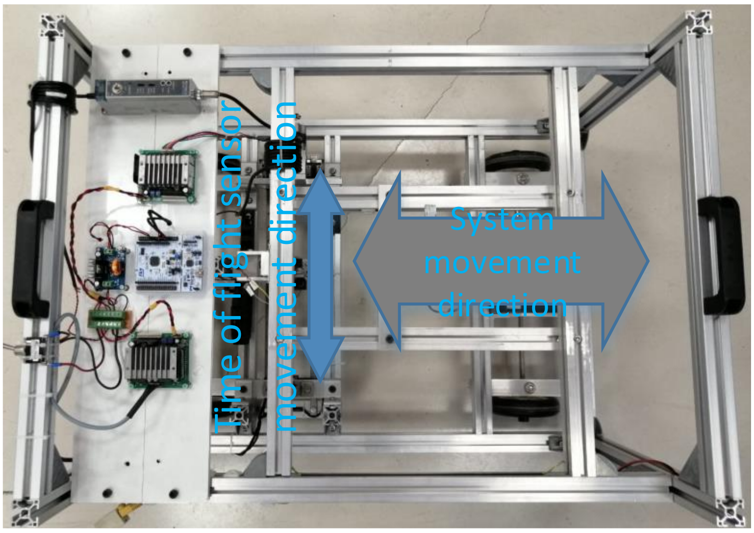

Figure 12. Movement axes of the entire mechanism and the ToF sensor

In the part that moves the ToF sensor, the shaft of the step motor and the slide screw are coupled to each other. As the slide screw rotates, the ToF sensor moves back and forth. When the step motor connected to the slide screw takes one step, the ToF sensor moves 0.05 mm (Eq. 2.5). This is an important criterion for the measurement range accuracy of the ToF sensor. This value can be changed by the frequency of the PWM (pulse width modulation) signal given to the ToF sensor by the microcontroller.

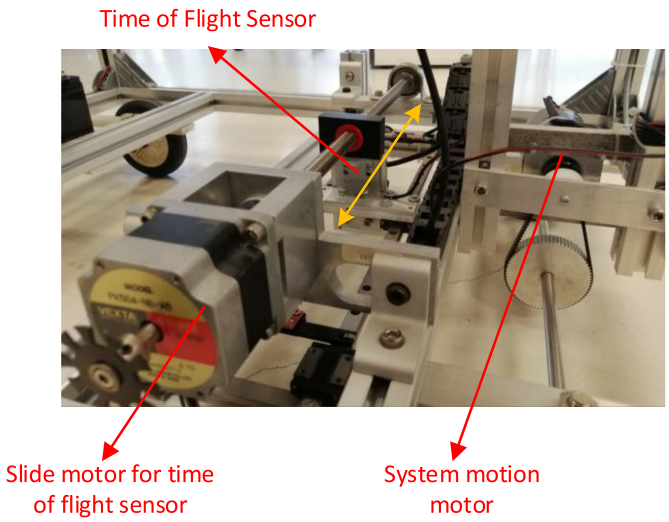

Figure 13. ToF and system motion mechanisms

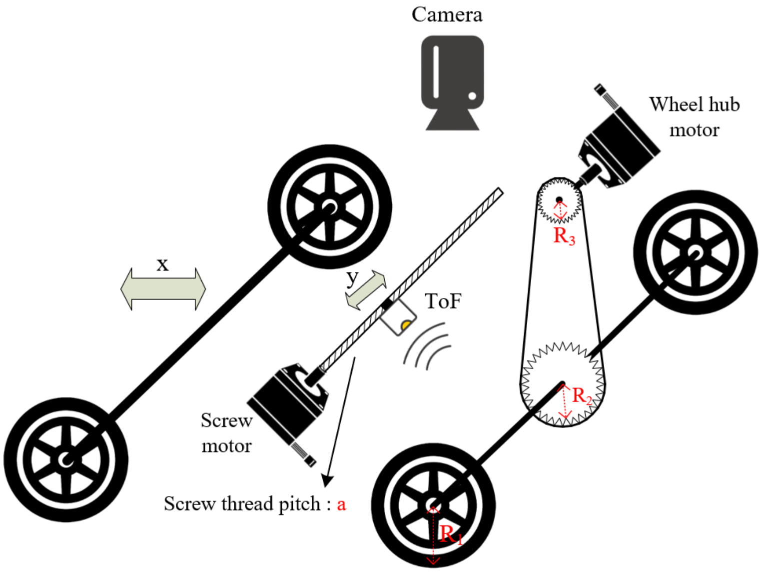

Figure 14. Screw and Pulley System

$$\mathrm{x} = \frac{2\pi . \mathrm{R}_1 . \mathrm{n}_{\text{wheel mot}} . \mathrm{R}_3}{\mathrm{R}_2} \tag{2.1}$$

$$\mathrm{R}_1 = 64 \text{ mm} \ , \quad \mathrm{R}_2 = 32 \text{ mm} \ \ , \quad \mathrm{R}_3 = 8 \text{ mm} \tag{2.2}$$

$$\mathrm{x} = \frac{2\pi . 64 . \left(\frac{0.36°}{360°}\right) . 8}{32} = 0.1 \text{ mm} \tag{2.3}$$

$$\mathrm{y} = \mathrm{n}_{\text{screw mot}} . \mathrm{a} \tag{2.4}$$

$$\mathrm{y} = \left(\frac{0.72°}{360°}\right) \mathrm{x} 2.5 = 0.05 \text{ mm} \tag{2.5}$$

The project mechanism is designed for precise and accurate movement, as it is used for measurement and sensing applications. The use of aluminum profiles and careful positioning of electronic components ensures stability and reduces vibration during movement. The pulley drive system and slide screw mechanism provide precise movement control for the wheels and TOF sensor, respectively.

2.2. System Architecture

The project system consists of a system that moves in a single direction. It performs real-time 3D reconstruction during its movement. The main units used in the project are listed below.

- Two Step Motor
- Two Motor Driver
- IP Block Camera and Camera Interface Board
- STM32 ARM Microcontroller
- Time of Flight Sensor
- Two Laser Stripe
- Two Limit Switch
- RS232-TTL and USB-RS232 Converter

While one stepper motor is used to provide movement in one direction for the system, the other stepper motor is used to enable the ToF sensor to move perpendicular to the direction of the system's movement. The system moves to scan the object for 3D reconstruction. The HD CMOS block camera is positioned at the upper-center point of the system (Figure 11). Images from this camera are transferred to the computer unit via 100 Mbps Ethernet. Additionally, two stripe lasers are positioned on both sides of the camera (parallel to the system's motion direction) at specific angles and distances. All controls of the system are performed through an ARM processor-based STM32 board. The drivers of the two stepper motors are controlled by the STM32 board. The STM32 board also reads the analog data produced by the TOF sensor with ADC peripheral. These analog values are then transferred to the computer where the images are processed via RS232 serial communication protocol. Two limit sensors have been used for the slide limits on the TOF sensor. Information about the TOF sensor reaching the limit sensors is also transferred to the computer unit via RS232 communication protocol. When the TOF Sensor motor activates these limit switches, it changes the direction of motion. The STM32 board also reads the IO signals of these switches.

The system is powered by 24 volts, which is provided by two 12-volt batteries. Two separate power converter boards are used for the power supply of the STM32 board and the camera. One of the converters is used as a 24V-12V converter for the camera board, while the other is used as a 24V-5V converter for the STM32 board and lasers. The motor drivers and ToF sensor are directly powered by the batteries at 24 volts.

ToF sensor scanning and laser scanning are carried out in two different system movements. During the first scan mode, laser data is collected, while during the second scan mode, ToF sensor data is collected. In laser scanning, the system is moved at a certain speed. Throughout this movement, a 25 fps video recording is captured by the computer unit. When the laser scanning process is completed, the video frames are separated and transferred to the 3D reconstruction database. The system speed can be reduced or the video fps value can be increased to perform a more precise scanning process.

In the second scanning process, the system moves a certain amount when the ToF sensor reaches any limit switch. The ToF sensor scanning continues until the entire scanning area is covered. In order to achieve a more precise scanning in ToF sensor scanning, the movement distance of the ToF sensor at each limit switch should be reduced. Reducing the movement distance of the ToF sensor at each limit switch too much can increase the scanning time, so it is necessary to keep it at an optimum value. Slowing down the motion speed with a ToF sensor enhances the precision of 3D reconstruction by enabling the capture of a greater number of samples within a specific distance. An optimal speed should be determined for specific applications.

2.2.1. Step Motor

A step motor is a DC motor that turns step by step. It can achieve the desired positioning with open-loop control since it does not have feedback. The movement of the stepper motors is achieved through the interaction between the magnet (rotor) and the windings (stator) located inside them (Figure 15). The rotor is set in motion by providing electrical power to the positive and negative poles on the motor. The motor takes one step with a single pulse voltage. When an electric current is applied to the step motor, it generates torque due to the electric current. This situation increases the holding force of the motor (“Nucleo-F746ZG.” Mbed). Even if the process is completed, torque is provided but if the electrical current is cut off, the torque effect disappears.

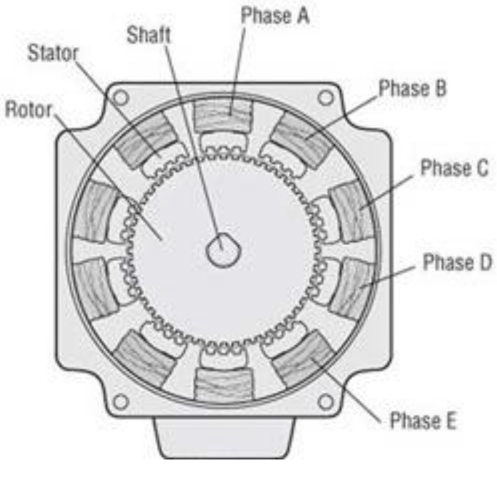

Figure 15. Motor structural Diagram

In the project, Vexta PK564-NB-A5 and PH569M-NAA model motors were used as shown in Figure 16. The nominal current values of both motors are 1.4 A. The motors are controlled by generating a PWM wave from the STM32 board. Each pulse of the PWM wave corresponds to one step movement of a motor. The rotation speed of the motors is determined by the frequency of the PWM wave. The higher the frequency, the higher the motor speed.

Figure 16. Vexta Step Motor

The stepper motor that moves the system completes 1000 steps per revolution, which corresponds to a steep angle of 0.36°. On the other hand, the stepper motor responsible for moving the TOF sensor slider completes 500 steps per revolution, resulting in a step angle of 0.72°.

2.2.2. Motor Driver

The step motor driver (Figure 17) used in the project is powered by a 24V power supply. It drives the connected step motor with a PWM signal. It moves with a given PWM signal at a specific frequency and duty cycle. The step motor advances one step with each pulse of the PWM waveform. The control of the motors is done through 4 lines connected to the MCU unit. These lines are PLS+, PLS-, DIR+, and DIR-. The PLS+ and PLS- input lines are connected to the PWM signal. When connecting to the PLS+ signal line, it is connected to the PLS- ground line. The DIR+ and DIR- lines determine the rotation direction of the motor. When a 3.3V digital output is applied to the DIR+ line, it moves in a clockwise direction. If a 3.3V digital output is applied to the DIR- line, it moves in the opposite direction (counterclockwise). The motor driver pulse waveforms are shown in Figure 18.

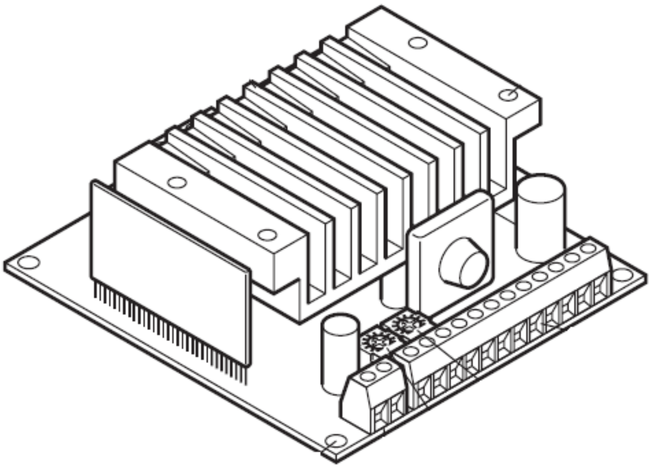

Figure 17. Step Motor Driver

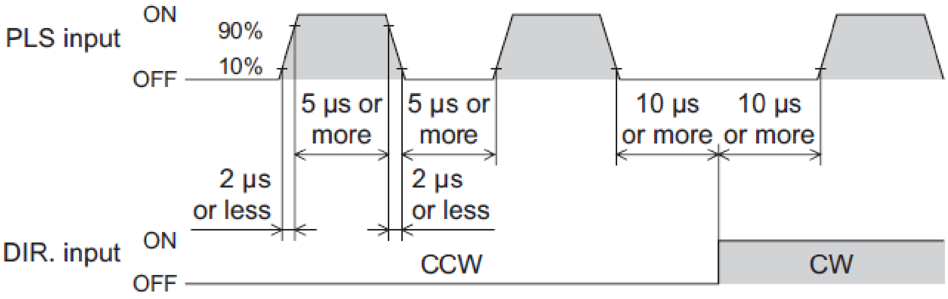

Figure 18. Step Motor Driver Pulse Waveform

2.2.3. IP Camera and Camera Interface Board

In the project, a Sony FCB-EV7520 color block camera is used (Figure 19). The camera uses a high-sensitivity 1/2.8-type Exmor R CMOS Sensor (2.13 megapixel) for image capture. The focal length value varies between 4.3 mm and 129 mm (30x optical zoom). Since the image is captured at the maximum zoom out value, the focal length is set to 4.3 mm. The 3D construction process is performed on HD (1280x720) images.

Additionally, the camera has WDR (wide dynamic range) and visibility enhancer (VE) features, which enable the camera to perform well in different lighting conditions.

The noise reduction (NR) feature is also used to minimize the salt-pepper noise effect that may occur in low-light environments.

An interface board is used with the camera to encode the digital image. The encoded digital image is transferred to the computer unit via a 100Mbit Ethernet connection. The zoom and focus settings of the camera are also adjusted through the Ethernet connection. The images are processed instantly by the computer unit. In addition, the power supply of the camera interface card is 12V. The 12V power is obtained by stepping down the 24V voltage that is taken from the batteries using voltage converters.

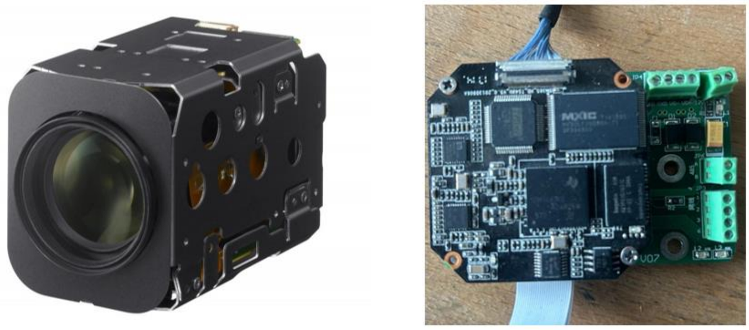

Figure 19. Sony Ip Block Camera and Ip interface Board

2.2.4. STM32 Microcontroller

STM32 is a family of microcontrollers that use ARM-based processors. In the project, STM32's Nucleo board produced by the STM32 company is used (Figure 20). The board is designed with a low power consumption and high-performance processor (216 MHz max CPU frequency). The processor used in the board is the F46ZG model from the F7 series of the STM32 family (“Nucleo-F746ZG.” Mbed, 2023).

The STM32 Nucleo board is a low-cost development board based on the STM32 microcontroller. Some of its features are (“Nucleo-F746ZG.” Mbed, 2023).:

- MCU: STM32 microcontroller in LQFP64 package
- Power supply: 5V USB or external source (3.3V, 5V, 7-12V)
- On-board ST-Link debugger/programmer with SWD connector

- Flexible power supply options with an on-board voltage regulator
- Two types of extension resources:
- ST morpho extension pin headers for full access to all STM32 I/Os
- Integrated ST-LINK/V2-1 debugger/programmer
- USB communication (Micro-USB connector)
- Three user LEDs, one user button
- Reset button with a blue LED as a status indicator
- Two onboard operational amplifiers (op-amps)
- One onboard digital-to-analog converter (DAC)
- One onboard analog-to-digital converter (ADC) with 12-bit resolution and up to 16 channels
- Multiple clock sources: HSE, LSE, HSI, LSI, PLL, and internal RC.

The programming of the following operations has been done with the Nucleo board in the project:

- Control of motors with drivers
- Reading the analog data of a ToF sensor with 12-bit precision.
- Transfer (with UART/RS232 communication) of external unit data to the computer unit
- Reading limit sensors digitally

Two PWM waves were generated separately by the microcontroller for the two motor drivers. The output voltage line of the ToF sensor was connected to the microcontroller's ADC peripheral line. The analog value of the connected line was converted to a digital value with a resolution of 12 bits. Then, these values were sent to the computer unit via the TTL-RS232 converter (Figure 27) connected to the board's UART line. The digital values of the limit switches, which are used to determine the motion limits of the TOF sensor, are read as 0-3.3V and the direction of the TOF sensor's step motor is changed accordingly. All of these operations are performed by the microcontroller.

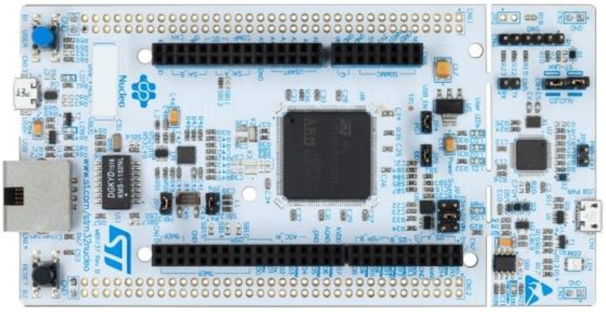

Figure 20. STM32 Nucleo Board

2.2.5. Time of Flight Sensor

The Time of Flight (ToF) principle is a method for measuring the distance between a sensor and an object based on the time difference between the emission of a signal and its return to the sensor after being reflected by the object. TOF sensors operate on this principle.

As shown in Figure 21, the sensor consists of a transmitter and a receiver. By calculating the round-trip time of the wave that hits the object in front of the sensor, it precisely determines the distance between the object in front of the sensor and the sensor itself.

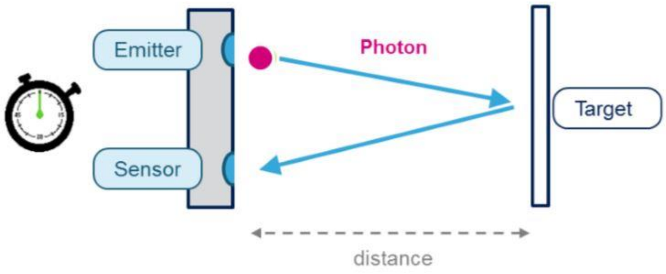

Figure 21. Time-of-Flight Principle (Source: (Brandao and Pedro, 2020))

$$\text{Measured Distance} = \frac{\text{Photon Travel Time}}{2} \text{ x Speed of light} \qquad (2.6)$$

The long-range model (LB-70) of Keyence's LB series (Figure 15) was used in the project. It measures with a precision of 10μm and has a measuring distance of 60mm-140mm (Figure 22). The distance response time is 40ms.

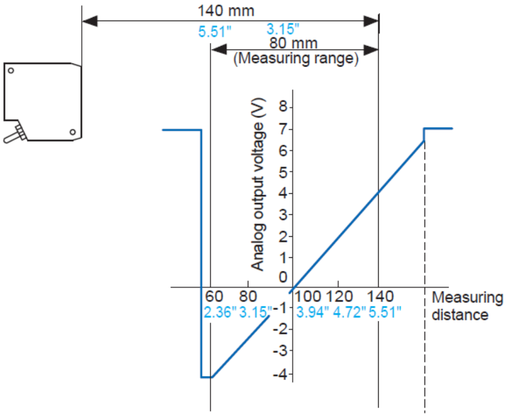

Figure 22. Measuring distance vs. analog output voltage

The LB-70 sensor (Figure 23) operates with a supply voltage between 12-24V. It is powered by 24V obtained from batteries. The distance measurement is read as an analog voltage from the sensor output line. The voltage value to be read is between -4 V to +4 V. As shown in Figure 22, the voltage value changes linearly according to the distance.

Figure 23. Keyence's LB70

2.2.6 Laser Stripe

In the project, two laser stripes were used as shown in Figure 24. The red laser stripe is a line emitting laser with 650nm wavelength and 5mW output power. The lasers are powered by 5V. Their power supply is provided through a 24V-5V voltage converter.

Figure 24. Laser Stripe

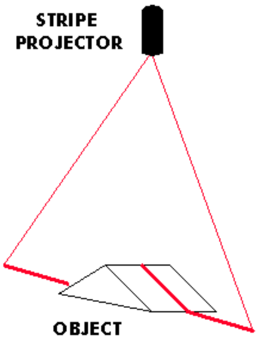

Figure 25. Stripe Projector

2.2.7. Limit Switches

Limit switches are used at the limits of the ToF sensor slide. These limit switches (Figure 26) allow the step motor to move in the opposite direction when it reaches the limit. The outputs of the switches are read by the STM32.

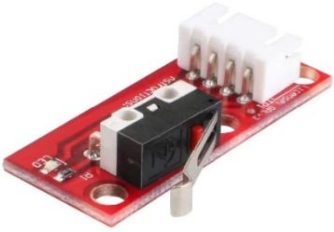

Figure 26. Limit Switch

2.2.8. RS232-TTL Converter

RS232-TTL converter (Figure 27) is a device that is commonly used to convert RS232 signals to TTL signals and vice versa. It is typically used in embedded systems such as microcontrollers to communicate with other devices that use different signal levels. The converter usually has a female DB9 connector on the RS232 side and a male 6-pin header on the TTL side. It requires a power supply of either 3.3V or 5V depending on the model and can support data transfer rates up to 115200 bps.

The RS232-TTL converter is used to convert the TTL voltage level of the microcontroller to the RS232 voltage level. The RS232 output of the converter is connected to a RS232-USB converter cable (Figure 28) to allow communication with a computer unit. Data transfer is carried out at a baud rate of 115200 bps. The ToF sensor values are transmitted in real-time through this communication channel, enabling real-time 3D reconstruction.

Figure 27. TTL-RS232 Converter

Figure 28. RS232-USB Converter

2.3. System Connections

The connections between the units in the project are shown in Figure 29. The motors are controlled through motor drivers with the microcontroller. Additionally, the analog values provided by the time-of-flight sensor's output are read by the ADC peripheral. The computer unit provides a connection to both the camera interface board and the microcontroller. The camera image is transferred to the computer unit via 100 Mbit Ethernet on the camera interface. Furthermore, the necessary ToF sensor information for processing in the computer unit is transmitted via RS232 serial communication. Power supply for the units is also provided by voltage converters.

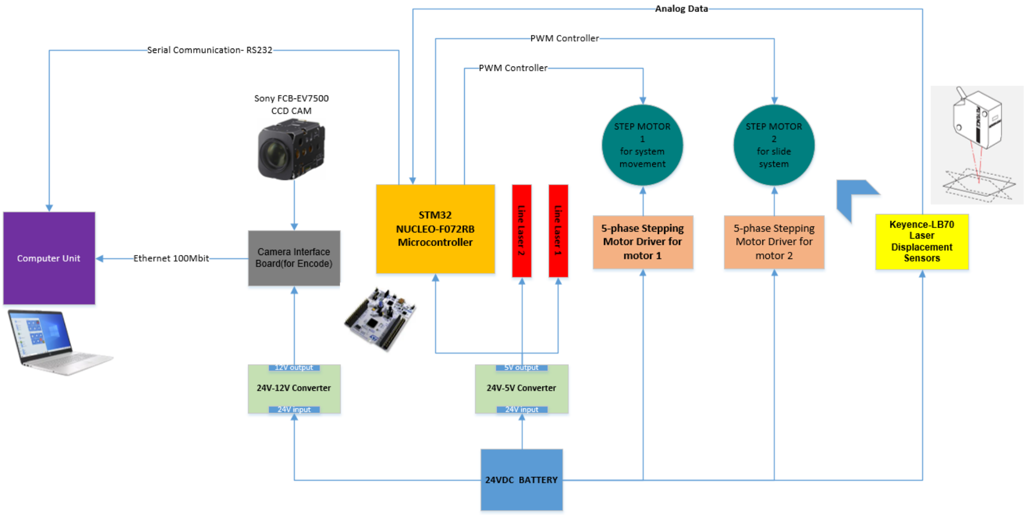

Figure 29. Schematic Diagram of Systems

2.4. Computer Programs

In the project, three software and interface programs were used, namely Matlab, STM32IDE, and Docklight Serial Monitor.

2.4.1. Matlab

Matlab is a high level programming language and environment that is widely used in scientific and engineering applications. It provides a flexible and interactive environment for numerical computation, data analysis, visualization and algorithm development.

One of the key features of Matlab is its extensive set of built-in functions and toolboxes, which cover various areas such as signal processing, image processing, control systems, optimization, and machine learning. These libraries enable users to perform complex tasks efficiently without having to write extensive code from scratch.

2.4.2. STM32IDE

STM32IDE is an integrated development environment developed by STMicroelectronics for developing applications on STM32 microcontrollers. STM32 microcontrollers are powerful and versatile microcontrollers that are widely used in various application areas such as consumer electronics, automotive and industry.

With STM32IDE, users can create projects, develop software, and debug applications for STM32 microcontrollers. The IDE offers a code editor, compiler, debugging tool, and project management features. It supports programming languages such as C and C++, allowing you to write efficient code for STM32 microcontrollers.

STM32IDE offers an easy-to-use interface and features that streamline the development process. It offers libraries, examples and documentation for quick project setup. The IDE also supports hardware debugging features that allow developers to monitor and analyze their applications on STM32 microcontrollers.

Overall, STM32IDE provides an efficient and practical development environment for building applications on STM32 microcontrollers and has therefore become a popular choice among developers.

2.4.3. Docklight Serial Monitor

Docklight Serial Monitor is a software tool used for monitoring, analyzing, and testing serial communication protocols. It supports various interfaces like RS232, RS485, RS422, and USB. With its user-friendly interface, users can monitor and log serial data, send custom commands, and perform comprehensive testing and analysis. It is widely used in industries such as automation, automotive, electronics, and telecommunications for diagnosing communication issues and ensuring reliability.

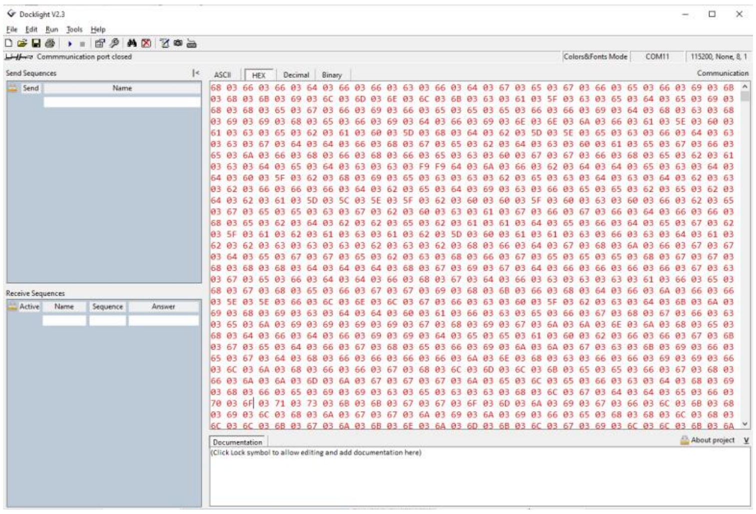

Commmunication port closed

Colors&Fonts Mode | COM11 | 115200, None, 8, 1

```
68 03 66 03 66 03 64 03 66 03 66 03 63 03 66 03 64 03 67 03 65 03 67 03 66 03 65 03 66 03 69 03 6B
03 68 03 6B 03 69 03 6C 03 6D 03 6E 03 6C 03 6B 03 63 03 61 03 5F 03 63 03 65 03 64 03 65 03 69 03
68 03 68 03 65 03 67 03 66 03 69 03 66 03 65 03 65 03 65 03 66 03 66 03 69 03 64 03 68 03 63 03 68
03 69 03 69 03 68 03 65 03 66 03 69 03 64 03 66 03 69 03 6E 03 6E 03 6A 03 66 03 61 03 5E 03 60 03
61 03 63 03 65 03 62 03 61 03 60 03 5D 03 68 03 64 03 62 03 5D 03 5E 03 65 03 63 03 66 03 64 03 63
03 63 03 67 03 64 03 64 03 66 03 68 03 67 03 65 03 62 03 64 03 63 03 60 03 61 03 65 03 67 03 66 03
65 03 6A 03 66 03 68 03 66 03 68 03 66 03 65 03 63 03 60 03 67 03 67 03 66 03 68 03 65 03 62 03 61
03 63 03 64 03 65 03 64 03 63 03 63 03 F9 F9 64 03 6A 03 66 03 62 03 64 03 64 03 65 03 63 03 64 03
64 03 60 03 5F 03 62 03 68 03 69 03 65 03 63 03 63 03 62 03 65 03 63 03 64 03 63 03 64 03 62 03 63
03 62 03 66 03 66 03 66 03 64 03 62 03 65 03 64 03 69 03 63 03 66 03 65 03 65 03 62 03 65 03 62 03
64 03 62 03 61 03 5D 03 5C 03 5E 03 5F 03 62 03 60 03 60 03 5F 03 60 03 63 03 60 03 66 03 62 03 65
03 67 03 65 03 65 03 63 03 67 03 62 03 60 03 63 03 61 03 67 03 66 03 67 03 66 03 64 03 66 03 66 03
68 03 65 03 62 03 64 03 62 03 62 03 65 03 62 03 61 03 61 03 64 03 65 03 66 03 64 03 65 03 67 03 62
03 5F 03 61 03 62 03 61 03 63 03 61 03 62 03 5D 03 60 03 61 03 61 03 63 03 66 03 63 03 64 03 61 03
62 03 62 03 63 03 63 03 63 03 62 03 63 03 62 03 68 03 66 03 64 03 67 03 68 03 6A 03 66 03 67 03 67
03 64 03 65 03 67 03 67 03 65 03 62 03 63 03 68 03 66 03 67 03 65 03 65 03 65 03 68 03 67 03 67 03
68 03 68 03 68 03 64 03 64 03 64 03 68 03 67 03 69 03 67 03 64 03 66 03 66 03 66 03 66 03 67 03 63
03 67 03 65 03 66 03 64 03 64 03 66 03 68 03 67 03 64 03 66 03 63 03 63 03 63 03 61 03 66 03 65 03
68 03 67 03 68 03 65 03 66 03 67 03 67 03 69 03 68 03 6B 03 66 03 68 03 64 03 66 03 6A 03 66 03 66
03 5E 03 5E 03 66 03 6C 03 6E 03 6C 03 67 03 66 03 63 03 60 03 5F 03 62 03 63 03 64 03 6B 03 6A 03
69 03 68 03 69 03 63 03 64 03 64 03 60 03 61 03 66 03 63 03 65 03 66 03 67 03 68 03 67 03 66 03 63
03 65 03 6A 03 69 03 69 03 69 03 69 03 67 03 68 03 69 03 67 03 6A 03 6A 03 6E 03 6A 03 68 03 65 03
68 03 64 03 66 03 64 03 66 03 69 03 69 03 64 03 65 03 65 03 61 03 60 03 62 03 66 03 66 03 67 03 6B
03 67 03 65 03 64 03 66 03 67 03 68 03 65 03 66 03 69 03 6A 03 6A 03 67 03 63 03 6B 03 69 03 66 03
65 03 67 03 64 03 68 03 66 03 66 03 66 03 66 03 6A 03 6E 03 68 03 63 03 66 03 66 03 69 03 69 03 66
03 6C 03 6A 03 68 03 66 03 66 03 67 03 68 03 6C 03 6D 03 6C 03 6B 03 65 03 65 03 66 03 67 03 68 03
66 03 6A 03 6A 03 6D 03 6A 03 67 03 67 03 67 03 6A 03 65 03 6C 03 65 03 66 03 63 03 64 03 68 03 69
03 68 03 66 03 65 03 69 03 69 03 63 03 65 03 63 03 63 03 68 03 6C 03 67 03 64 03 64 03 65 03 66 03
70 03 6F 03 71 03 73 03 6B 03 6B 03 67 03 67 03 6F 03 6D 03 6A 03 69 03 67 03 66 03 6C 03 6B 03 68
03 69 03 6C 03 68 03 6A 03 67 03 67 03 6A 03 69 03 6A 03 69 03 66 03 65 03 68 03 68 03 6C 03 68 03
6C 03 6C 03 6B 03 67 03 6A 03 6B 03 6E 03 6A 03 6D 03 6B 03 6C 03 67 03 69 03 6C 03 6C 03 6B 03 6A
```

(Click Lock symbol to allow editing and add documentation here)

Figure 30. Docklight Serial Interface

CHAPTER 3

MATHEMATICAL APPROACHES

3.1. Double Laser Triangulation System

3.1.1. Construction Point Cloud

Laser Triangulation method is a widely used system for 3D scanner systems. Laser and camera positioning can be different according to the applications. In this study, a camera with two laser stripes and a pinhole camera model was used. System performance may vary depending on laser light form and camera resolution (Ozan and Sevket Gumustekin, 2012). Calculation is shown on a single laser for a better understanding of the subject. Then the same process will be used for the other laser (right or left laser stripe) (Munaro, et al., 2015).

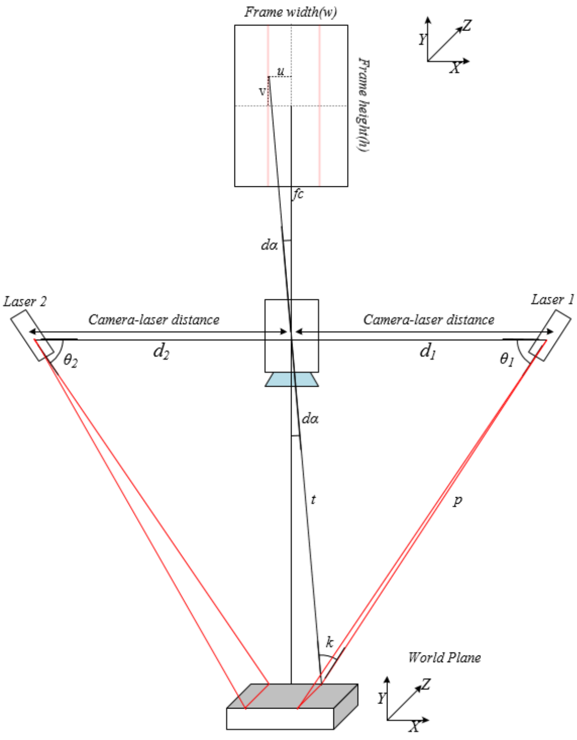

Figure 31. Two laser stripe Triangulation System

As shown in Figure 31, triangulation system can be mainly described by baseline d and laser angle θ. The baseline d value indicates the distance between the camera and laser diode. The laser angle θ respresents the angle of the laser plane to the camera sensor plane.

Intrinsic parameters obtained from camera calibration results are in calculations.

- o_x and o_y : the pixel coordinate of the image center (principal points)
- f_c: the focal length
- s_x and s_y : the effective size of pixel (horizontal and vertical direction)

In the specification of the camera, the frame size and the FOV(field of view) value of the camera lens are known. HD image of size 1280x720 using an ethernet camera is obtained. The widest field of view value of the zoom lens was used in the experiments which is 63.7 degrees.

The triangle on which the operations will be performed consists of p, t and d side lengths.

- p : It is the distance between any pixel where the laser is detected and the laser diode.
- t : It is the distance between any pixel where the laser is detected and the camera center.
- d: It is the distance between camera sensor and laser diode.

In addition, the μ and v values on the frame give the vertical and horizontal length of the laser line to the frame midpoint, as shown in Figure 31.

Firstly, the focal length value needs to be calculated using frame width, effective size of pixel and field of view.

$$\tan\left(\frac{\text{Field of View}}{2}\right) = \frac{\left(\frac{\text{frame with}}{2}\right)\text{x size of pixel}}{\text{focul lenght (fc)}} \tag{3.1}$$

$$\text{fc} = \frac{\left(\frac{1280}{2}\right)\ \text{x}\ 4.35\ \mu\text{m}}{\tan\left(\frac{63.7°}{2}\right)} = 4.48\ \text{mm} \tag{3.2}$$

The triangulation method used in the laser triangulation system is based on the law of sines, which is a fundamental trigonometric principle (So, et al., 2012). The following trigonometric equation is obtained when the triangle law of sine is applied by using the triangle formed between laser diode, focal point of the camera and object (Žbontar, et al., 2013).

$$\frac{\mathrm{d_1}}{\sin(\mathrm{k})} = \frac{\mathrm{p}}{\sin\left(\frac{\mu}{2} - \mathrm{d}\alpha\right)} = \frac{\mathrm{t}}{\sin(\theta)} \tag{3.3}$$

These angles are related by:

$$\mathrm{k} + \frac{\mu}{2} - \mathrm{d}\alpha + \theta = \mu \tag{3.4}$$

which gives us

$$\mathrm{k} = \frac{\mu}{2} + \mathrm{d}\alpha - \theta \tag{3.5}$$

and, equation of side t length using equation 3.3 is:

$$\frac{\mathrm{d_1}}{\sin(\mathrm{k})} = \frac{\mathrm{t}}{\sin(\theta)} \tag{3.6}$$

$$\mathrm{t} = \frac{\mathrm{d_1} \,.\, \sin(\theta)}{\sin(\mathrm{k})} \tag{3.7}$$

After determining the t and k variable, the equation of angle dα is defined using relationship between camera plane and image plane.

$$\tan(\mathrm{d}\alpha) = \frac{\mathrm{u} \,.\, \mathrm{sz_{px}}}{\mathrm{f_c}} \tag{3.8}$$

$$\mathrm{d}\alpha = \arctan\left(\frac{\mathrm{u} \,.\, \mathrm{sz_{px}}}{\mathrm{f_c}}\right) \tag{3.9}$$

Finally, the equations of X, Y and Z axis points in the world coordinates corresponding to any laser stripe point are obtained.

$$\mathrm{Z} = \cos(\mathrm{d}\alpha)\ \mathrm{x}\ \mathrm{t} \tag{3.10}$$

$$\mathrm{Z} = \frac{\cos(\mathrm{d}\alpha)\,.\,\mathrm{d}_1\,.\,\sin(\theta)}{\sin\left(\frac{\pi}{2} + \mathrm{d}\alpha - \theta\right)} \tag{3.11}$$

$$\mathrm{X} = \mathrm{Z}\ \mathrm{x}\ \frac{\mathrm{u}\ \mathrm{x}\ \mathrm{sz}_{\mathrm{px}}}{\mathrm{f}_{\mathrm{c}}} \tag{3.12}$$

$$\mathrm{Y} = \mathrm{Z}\ \mathrm{x}\frac{\mathrm{v}\ \mathrm{x}\ \mathrm{sz}_{\mathrm{px}}}{\mathrm{f}_{\mathrm{c}}} \tag{3.13}$$

3.1.2. Depth Sensing Range

In 3D scanning systems, the depth sensing range is an essential issue. It refers to the highest and least depths that the system is capable of measuring reliably. $\mathrm{Z}_{\mathrm{min}}$ and $\mathrm{Z}_{\mathrm{max}}$ present the least and greatest depths that can be measured in the context of the system depicted in the Figure 32.

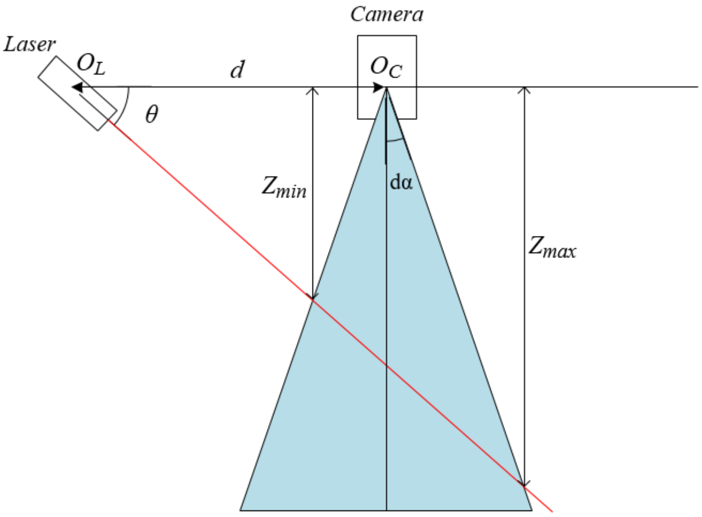

Figure 32. Depth Sensing Range of Laser Triangulation System

It is important to note that the depth sensing range isn't the same as the maximum range of the system. The maximum range refers to the distance between the scanner and the object being scanned, beyond which the system cannot capture any data. The depth sensing range, on the other hand, is the range within which the system can accurately measure depth information (Munaro, et al., 2015).

The laser and camera are located at $\mathrm{O_L}$ and $\mathrm{O_C}$ points as shown in the Figure 32. The value $\mathrm{d\alpha}$ is half the angle of the camera field of view. Triangulation angle is shown with θ between camera and laser principal axis. The maximum and minimum depth are measured with specified system are represented with $\mathrm{Z_{min}}$ and $\mathrm{Z_{max}}$.

Although two lasers are used in the project, since the angle values of the lasers are equal, calculations are made on a single laser for the depth sensing range.

$$\mathrm{Z_{min}} = \frac{\mathrm{d\ x}\sin(\theta)\mathrm{\ x}\cos\left(\frac{\mathrm{d\alpha}}{2}\right)}{\cos\left(\theta - \frac{\mathrm{d\alpha}}{2}\right)} = \frac{\mathrm{d}}{\frac{1}{\tan(\theta)} + \tan\left(\frac{\mathrm{d\alpha}}{2}\right)} \tag{3.14}$$

$$\mathrm{Z_{min}} = \frac{250\ \mathrm{mm}}{\frac{1}{\tan(60°)} + \tan\left(\frac{63.7°/2}{2}\right)} = 290\ \mathrm{mm} \tag{3.15}$$

$$\mathrm{Z_{max}} = \frac{\mathrm{d\ x}\sin(\theta)\mathrm{\ x}\cos\left(\frac{\mathrm{d\alpha}}{2}\right)}{\cos\left(\theta + \frac{\mathrm{d\alpha}}{2}\right)} = \frac{\mathrm{d}}{\frac{1}{\tan(\theta)} - \tan\left(\frac{\mathrm{d\alpha}}{2}\right)} \tag{3.16}$$

$$\mathrm{Z_{max}} = \frac{250\ \mathrm{mm}}{\frac{1}{\tan(60°)} - \tan\left(\frac{63.7°/2}{2}\right)} = 856\ \mathrm{mm} \tag{3.17}$$

The difference between the $\mathrm{Z_{min}}$ and $\mathrm{Z_{max}}$ value is the depth sensing range value.

$$\Delta \mathrm{Z} = \mathrm{d\ x}\sin\theta\mathrm{\ x}\cos\left(\frac{\mathrm{d\alpha}}{2}\right)\mathrm{x}\left(\frac{1}{\cos\left(\theta + \frac{\mathrm{d\alpha}}{2}\right)} - \frac{1}{\cos\left(\theta - \frac{\mathrm{d\alpha}}{2}\right)}\right) = \frac{2\mathrm{\ x\ d\ x}\tan\left(\frac{\mathrm{d\alpha}}{2}\right)}{\frac{1}{\tan^2(\theta)} - \tan^2\left(\frac{\mathrm{d\alpha}}{2}\right)} \tag{3.18}$$

$$\Delta \mathrm{Z} = 566\ \mathrm{mm} \tag{3.19}$$

The $\mathrm{Z_{max}}$ value in the calculation above represents the maximum depth that the camera-laser system can calculate. However, in the project, the distance from the camera center to the ground is 430 mm. Therefore, the $\Delta\mathrm{Z}$ value for our project is 140 mm, unless the cart is moved on a rail above ground.

It should be noted that, if triangulation angle θ and baseline d increase, Z_{min} and Z_{max} values increase but the depth measurement accuracy decrease.

3.1.3. Depth Resolution

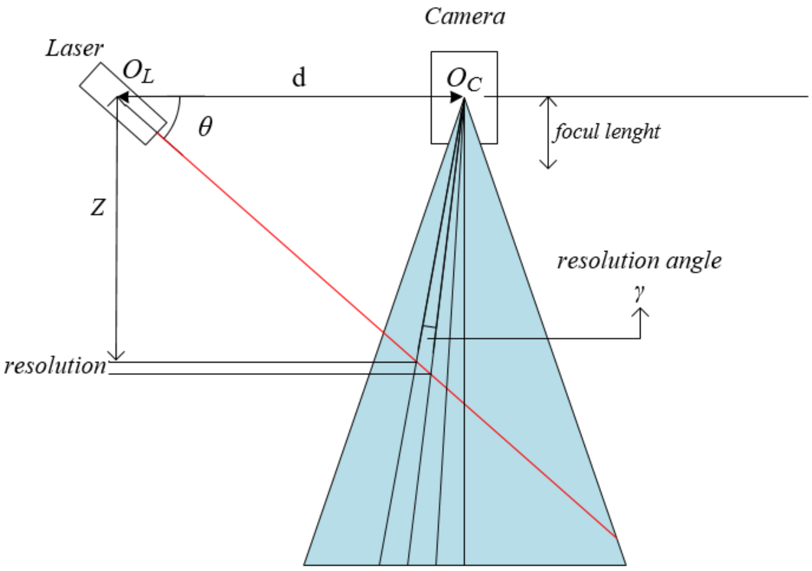

Figure 33. Depth Resolution in Laser Triangulation system

The resolution value changes according to the features of the camera used, and the triangulation angle between camera and laser. The resolution angle is related to focal length and effective pixel size. The resolution angle is $\gamma = \tan^{-1}\left(\frac{\mathrm{sz_{px}}}{\mathrm{f_c}}\right) = 0.0556°$.

$$\text{resolution} = \mathrm{Z\,x}\left(\frac{\cos(\theta)\ \mathrm{x}\cos(\gamma)}{\cos(\theta-\gamma)} - 1\right) = \mathrm{Z\,x}\frac{1}{\frac{1}{\tan(\theta)\ \mathrm{x}\tan(\gamma)} - 1} \tag{3.20}$$

$$= \mathrm{Z\,x}\frac{1}{\frac{1}{\tan(60°)\ \mathrm{x}\tan(0.0556°)} - 1} = \mathrm{Z\,x}\ 0.0017 \tag{3.21}$$

Thus, resolution depend on depth Z and triangulation angle θ values increase. While the upper points of the object are scanned with a more precise resolution, the lower parts are scanned with less resolution than the upper points. The resolution decreases as the depth Z and triangulation angle θ increase. If the triangulation angle is increased for precise resolution, depth sensing range is decreased. Therefore, an optimum triangulation angle should be determined according to the application. (Munaro, et al., 2015).

3.1.4. Occlusion Problem Statement

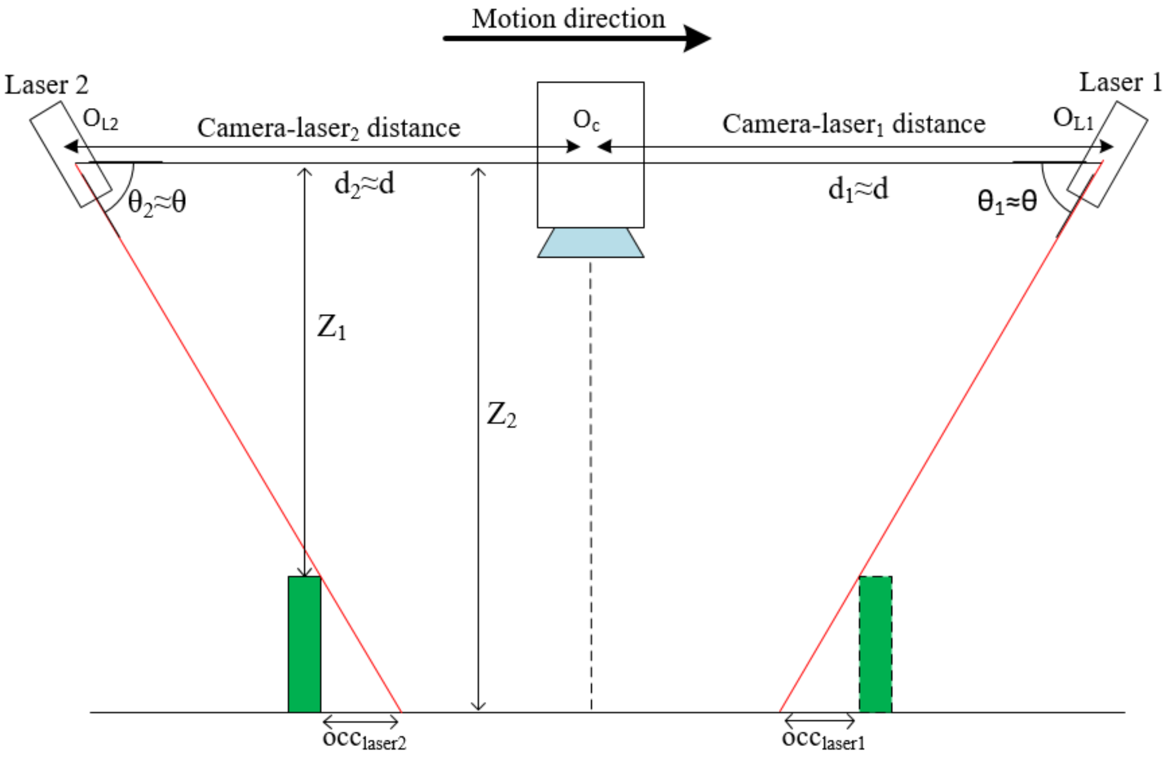

Figure 34. Occlusion First Scenario

As shown in Figure 34, laser line is blocked in a certain area around the object due to the object. Since two lasers are used in the camera laser system, the occlusion region for the laser is not problem. Because where there is no a laser, there is another laser (Peiravi, et al., 2007). This situation is seen in Figure 35.

The depth of the object and the distance of baseline axis to surface of the object are indicated by Z_1 and Z_2. For a given baseline d and triangulation angle θ, the laser occlusion path length can be found as :

$$occ_{laser} = \frac{Z_2 - Z_1}{\tan(\theta)} \tag{3.22}$$

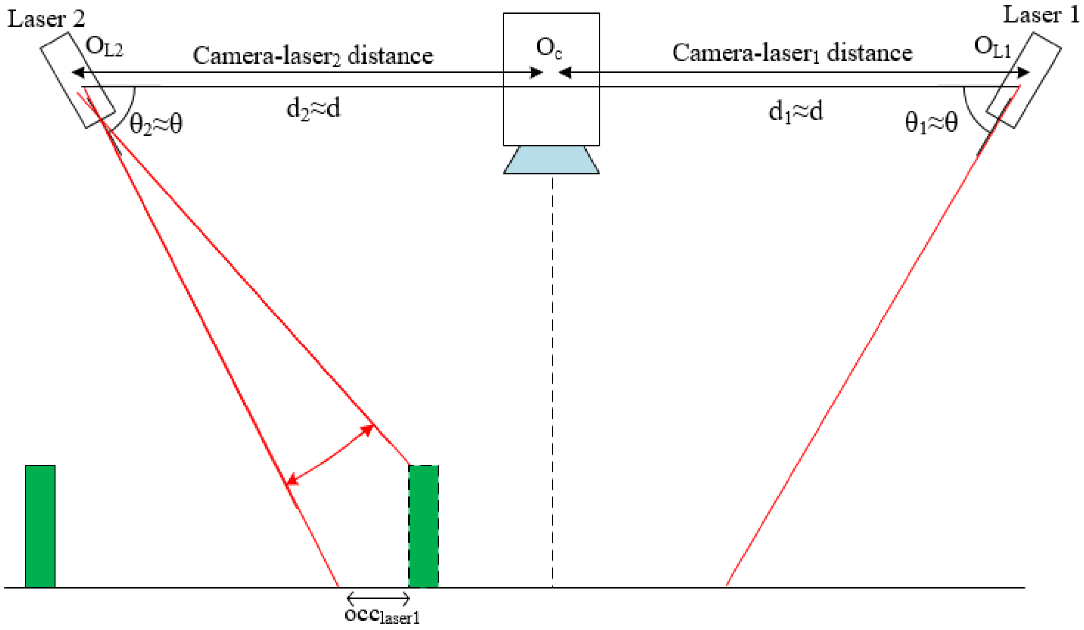

Figure 35. Occlusion Second Scenario

As shown in Figure 36, laser 2 reflect in occlusion region of the object which blocked by laser. Therefore, occlusion problem occurred by a single laser is solved by using two lasers. This is one of the main reasons for using two lasers.

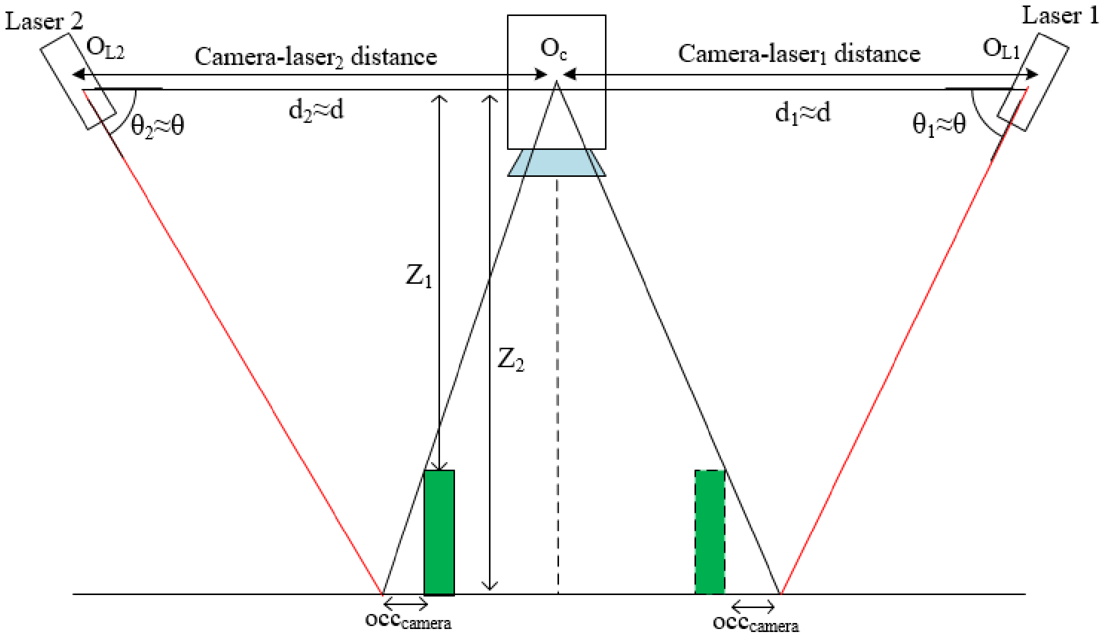

Figure 36. Occlusion Third Scenario

In additon, the occlusion region occurs because of the camera's field of view angle. Camera of occlusion region is represented by:

$$\mathrm{occ}_{\mathrm{camera}} = \left(1 - \frac{Z_2}{Z_1}\right) x(d - \frac{Z_2}{\tan(\theta)}) \qquad (3.23)$$

When the angle between the camera axis and the laser axis increases, the occlusion laser distance decreases, while the occlusion camera distance increases.

3.2. Camera Sensor Calibration

The camera calibration process is the essential part of every computer vision system designed for physical measurements. The image processing and image analysis stages performed with an uncalibrated camera contain errors (Chen, et al., 2021). Therefore, the camera should be calibrated and ready for image processing.

The internal parameters of the camera need to be determined via calibration process. "Matlab Toolbox for Camera Calibration" library is used for the calibration process.

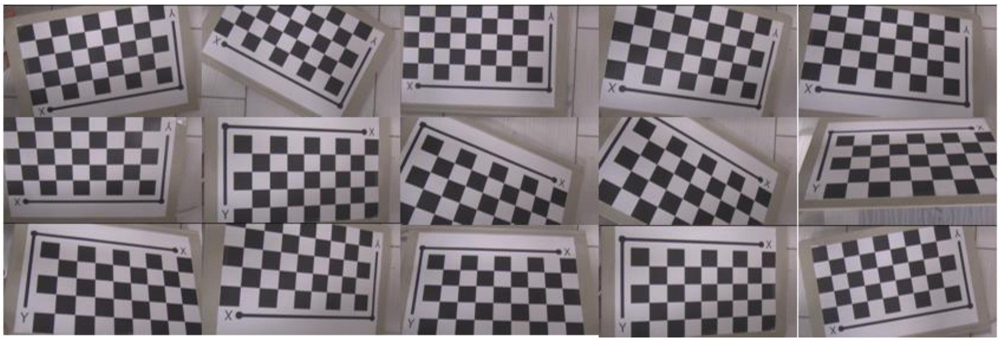

Figure 37. Chessboard Pattern Images

The chessboard images shown in figure 37 is used for the calibration process (Ntouskos, et al., 2007). The chessboard pattern pictures taken from different angles in appropriate lighting conditions were processed as calibration input. In figure 38, the camera and pattern centric illustrations are visualized.

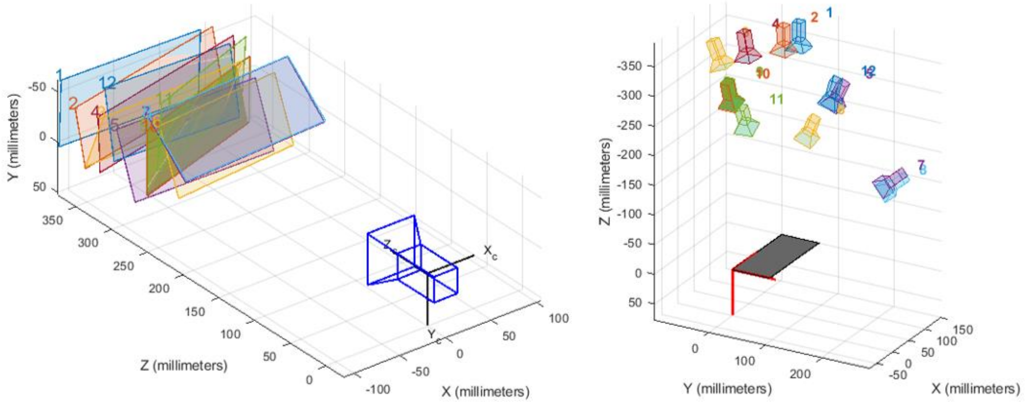

Figure 38. Pattern-centric and Camera-centric View

After this calibration, the following outputs are obtained as intrinsic parameters.

- Principal points(optical center) : ox, oy (unit of pixel size)
- Focal Length in pixels : fx, fy (unit of pixel)

The calibration results are shown as the intrinsic matrix as follows:

$$\begin{bmatrix} \mathrm{f_x} & 0 & \mathrm{o_x} \\ 0 & \mathrm{f_y} & \mathrm{o_y} \\ 0 & 0 & 1 \end{bmatrix} = \begin{bmatrix} 1028.84412 & 0 & 648.47410 \\ 0 & 1028.59061 & 363.64953 \\ 0 & 0 & 1 \end{bmatrix} \qquad (3.24)$$

The pixel size of the camera sensor used is 4.35 µm. The $\mathrm{f_x}$ and $\mathrm{f_y}$ values in equation 3.24 are in pixel units. When these values are multiplied by the pixel size, they are found to be very close to the theoretically calculated focal length (Eq. 3.2). Therefore, a focal length value of 4.48 mm was used for both axes (x and y) in all the studies. However, the $\mathrm{o_x}$ and $\mathrm{o_y}$ values obtained from calibration will be utilized in all calculations throughout the project.After processing the above outputs, images free from sensor noise and lens distortion are obtained.

3.3. Laser Path finding (in sub-pixel accuracy)

In the project, the image in RGB format is converted to gray-scale image format for the separation of laser light lines. In the RGB format image, the brightest points of the laser lines appear in white. The midpoint of the laser line is considered the brightest point.

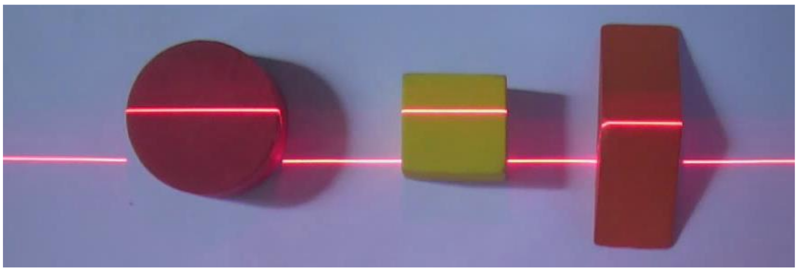

Figure 39. RGB image with laser stripe

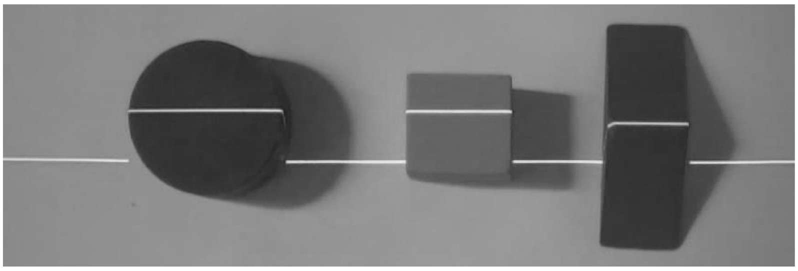

Figure 40. Gray-scale image with laser stripe

The image converted to gray-scale format has the highest gray value on each vertical axis. This process is repeated 1280 times for each image. In each iteration, two pixels (due to two laser stripes) with the highest gray-scale value are found from 720 pixels. In the Figure 41, laser stripe detection is shown in pixel resolution.

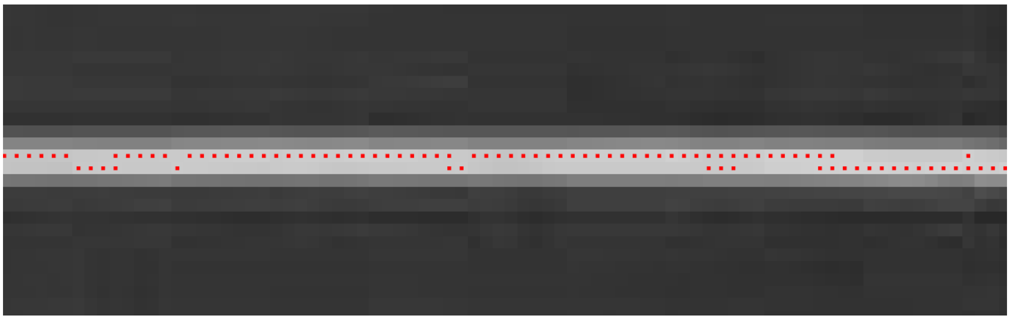

Figure 41. One pixel resolution (highest gray-scale value)

However, as a result of this process, the separated laser stripes are in one pixel resolution. The method of finding the highest pixel value poses certain disadvantages due to variations in the reflection of projected laser stripes under different lighting conditions, the fluctuating brightness of the laser, the non-straight paths of the laser stripes, and the processing performed at a single pixel resolution.

Gaussian distribution method was used to avoid the mentioned problems. According to this method, the vertical distribution of the laser lines is defined as the Gaussian distribution (Nguyen, et al., 1995). According to the Gaussian equation specified in equation 3.25, the parameter μ corresponds to the peak point of the Gaussian graph. This peak point gives the brightest point of the laser stripe. These obtained points provide sub-pixel resolution reconstruction.

$$f(x) = \frac{1}{\sigma\sqrt{2\pi}} e^{\frac{-(x-\mu)^2}{2\sigma^2}} \tag{3.25}$$

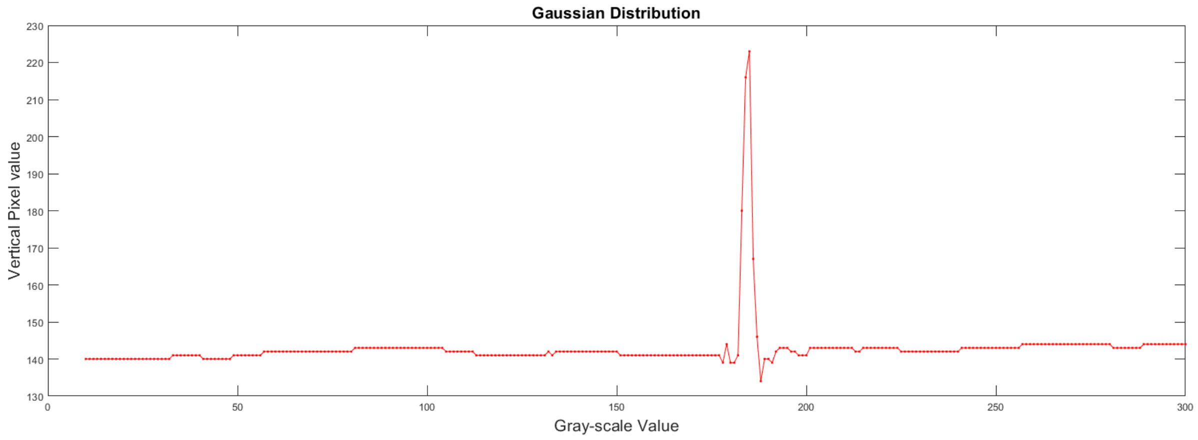

Figure 42. The distribution of the 300th horizontal pixel on which Gaussian function of fit

As can be seen in figure 43, a significant improvement was observed in the reconstruction thanks to the sub-pixel accuracy obtained.

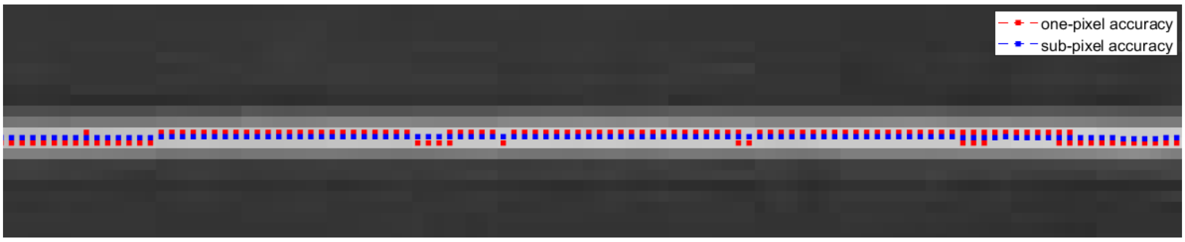

Figure 43. One-pixel Accuracy (red) vs. sub-pixel Accuracy (blue)

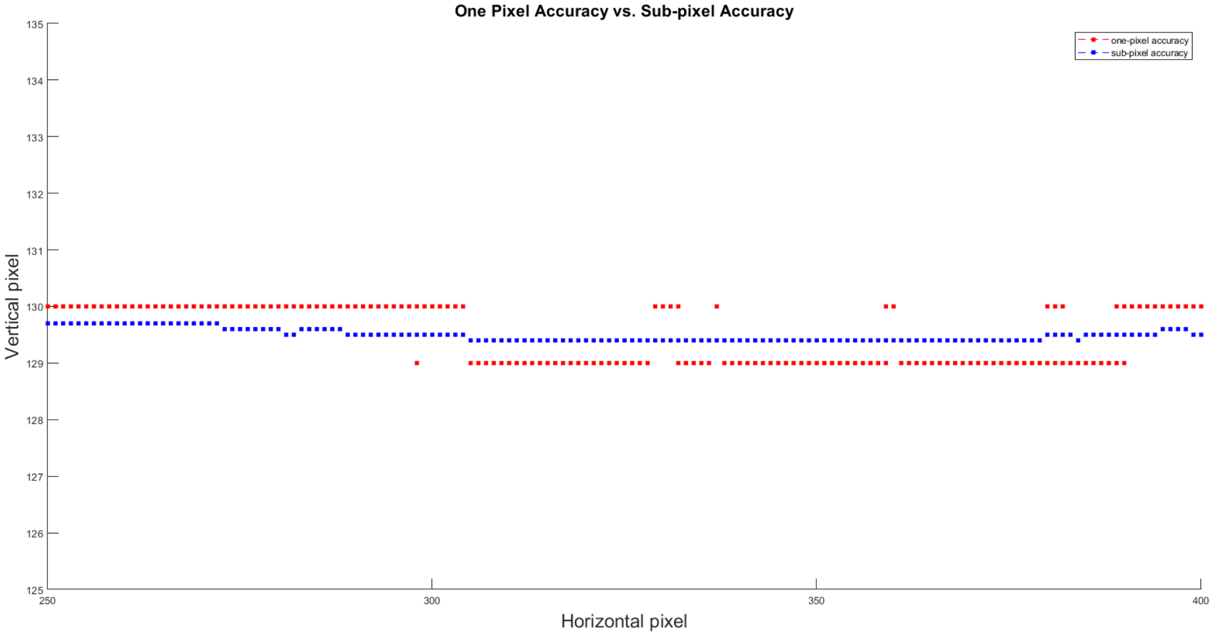

Figure 44. One-pixel Accuracy (red) vs. sub-pixel Accuracy (blue)

CHAPTER 4

OPTIMIZATION AND CALIBRATION

4.1. Laser Angle and Baseline Calibration with Time of Flight Sensor

System calibration is essential in order to achieve accurate alignment of the data obtained from the two laser sources in the scanning system through active triangulation. The positions between the camera and the lasers were measured using standard measuring tools, which is why the active triangulation outputs for the two lasers do not perfectly match (Lindner, et al., 2010). The reason for this is small errors that occur during measurement. Three different objects were used for the first scanning process, as shown in Figure 45. The calibration process is more effective when objects with sharp edges are used.

The ToF sensor used in the project operates at specific intervals to determine the real-time error margin in angle and distance values. These error margins may vary due to vibrations since the system operates continuously. The ToF sensor calculates these error margins in real-time, leading to changes in the values of the active triangulation method.

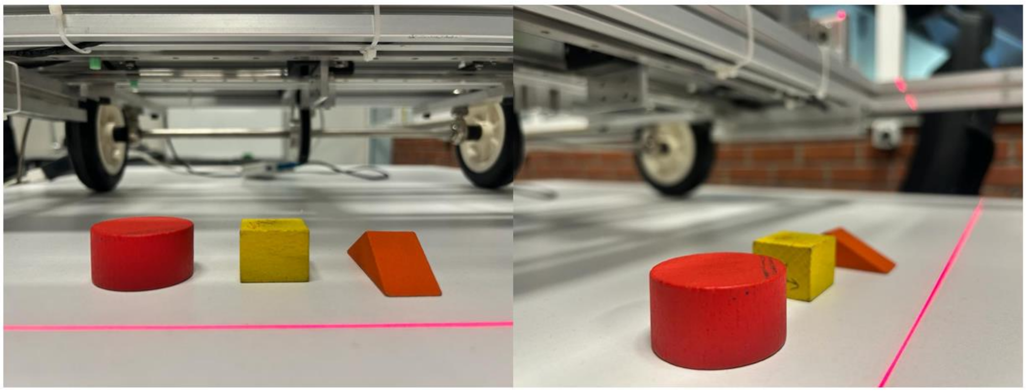

Figure 45. The positions of the three objects in workspace

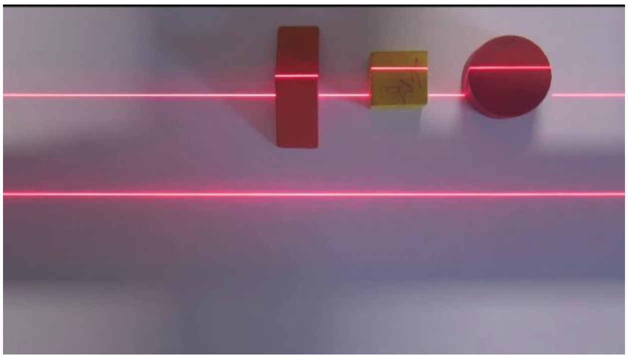

Figure 46. Camera Image during Scanning (Three Objects)

In order to automatically calibrate the accuracy of laser angles and distances to the camera, the point cloud obtained from the ToF sensor is used (Jung, et al., 2015). The ToF 3D point cloud shown in Figure 47 represents the real dimensions of the objects. Rectangular prism was used among the three objects to calibrate the distance between laser-camera (baseline) and the laser angle. This laser scanner outputs can also be seen in figures 48 and 49.

Two points indicating the height of the rectangular prism are selected from the ToF output. These points are used for the optimization algorithm to determine the $\mathrm{Z_{ToF}}$ value. Subsequently, the same points are marked in the 3D outputs obtained from laser 1 and laser 2, and separate optimization processes are performed for each. When examining the dimensions of the rectangular prism through its coordinates, the length, width, and height values are determined to be 25.4 mm, 24.2 mm, and 19.35 mm, respectively.

The outputs of laser-1 (Figure 48) and laser-2 (Figure 49) are calibrated based on the 3D output of the ToF sensor. Error margins in the measured values are determined. The error margins obtained after this calibration will be used for the following studies. The following units are referenced to Figure 31.

- Distance between laser-1 and camera optical center: $\mathrm{d_1}$
- The angle between laser-1 and the optical axis of the camera: θ_1
- Distance between laser-2 and camera optical center: $\mathrm{d_2}$
- The angle between laser-2 and the optical axis of the camera: θ_2

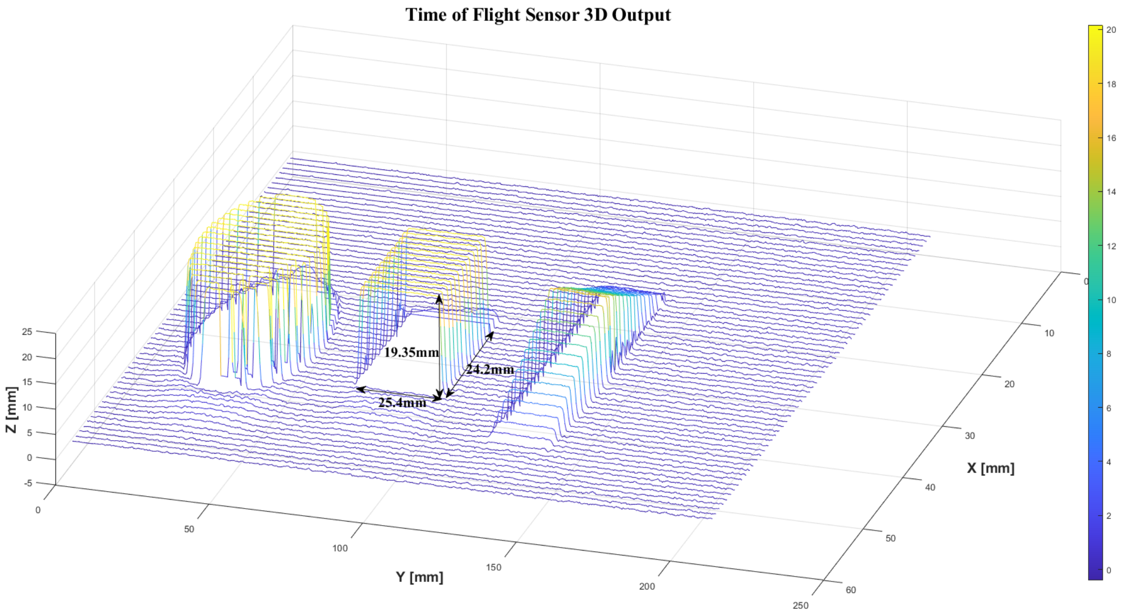

Figure 47. 3D Point Cloud of ToF (Three objects)

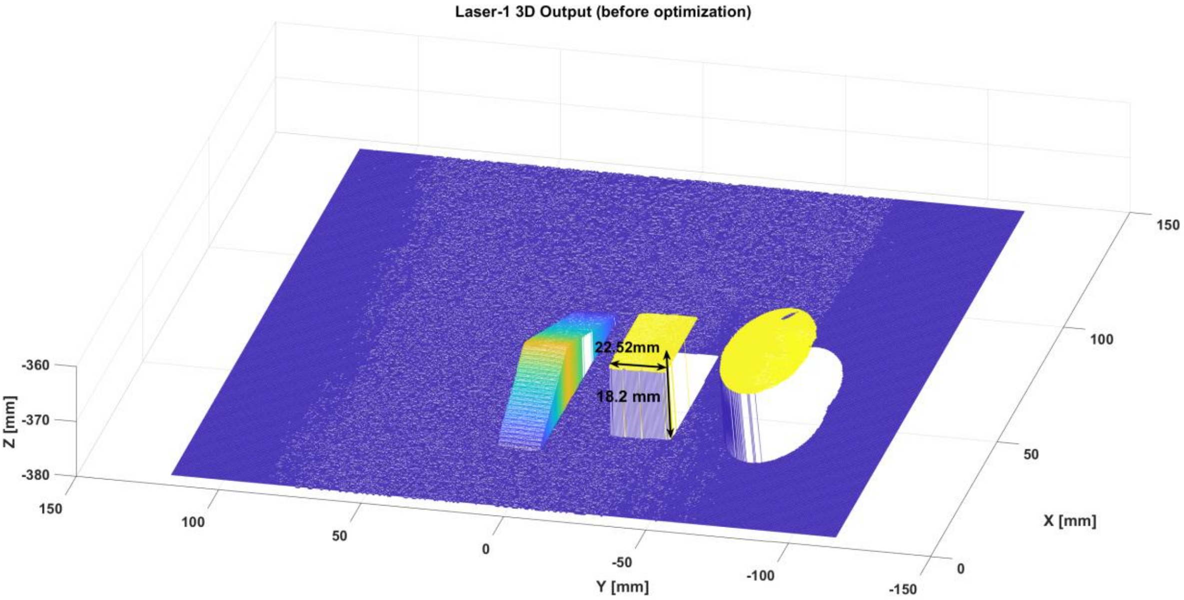

Figure 48. Laser-1 3D Output before Calibration

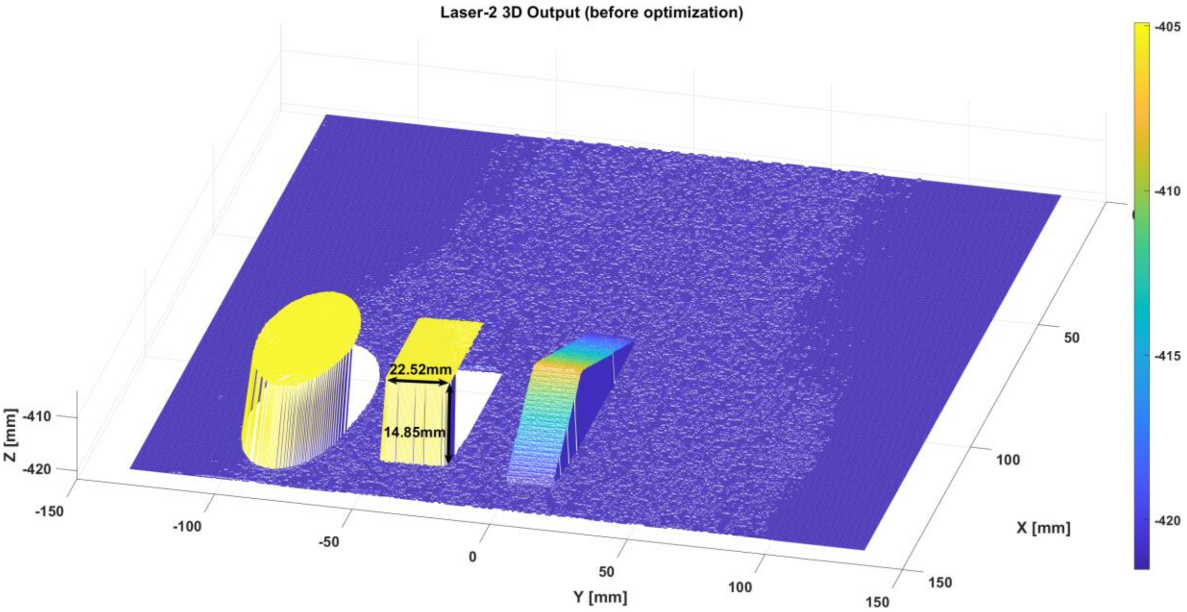

Figure 49. Laser-2 3D Output before Calibration

As shown in Figures 48 and 49, the dimensions of the 3D outputs obtained by active triangulation of laser-1 and laser-2 are not the same as the actual dimensions. The values obtained from the ToF sensor (Figure 47) were optimized using the Nelder-Mead algorithm based on laser angles and distance variables (Gao, et al., 2010). The objective functions in the optimization algorithm is represented by equation 4.1 and 4.2. This function aims to minimize the depth differences between the values obtained from the ToF sensor and the lasers. Since the variables X (Eq. 3.12) and Y (Eq. 3.13) depend on the variable Z (Eq. 3.11), the optimization process was performed solely on the Z objective function. Based on the optimization results, the laser values have been updated with the following error margins. It can be observed that these error margins also provide approximate values in the X and Y equations.

$$\mathrm{f}(\mathrm{d}_1, \theta_1) = \left|\mathrm{Z}_{\mathrm{ToF}} - \mathrm{Z}_{\mathrm{laser}_1}\right| \tag{4.1}$$

$$\mathrm{f}(\mathrm{d}_2, \theta_2) = \left|\mathrm{Z}_{\mathrm{ToF}} - \mathrm{Z}_{\mathrm{laser}_2}\right| \tag{4.2}$$

The d and θ variable parameters have been optimized using the Nelder-Mead algorithm with the values obtained from the ToF sensor. The measured values for angles and distances are 60° and 246 mm, respectively.

- θ_1 : 60° + 5.7536 °
- θ_2 : 60° + 2.4899 °
- d_1: 246 mm + 5.6284 mm
- d_2: 246 mm + 5.4805 mm

After the optimization process, an error margin of +5.7536° was found for laser 1 angle (θ_1), and an error margin of 2.4899° was found for laser 2 angle (θ_2). As for the distances between the camera and the lasers, values of +5.6284 mm (d_1) and +5.4805 mm (d_2) were determined, respectively. Based on the above values, the outputs of laser-1 and laser-2 have been shown in Figures 50 and 52 with the values closest to the actual size. The iteration graphs of the Nelder-Mead algorithm are shown in figures 51 and 53. The points on the graph represent the iteration points where the equation approaches zero.

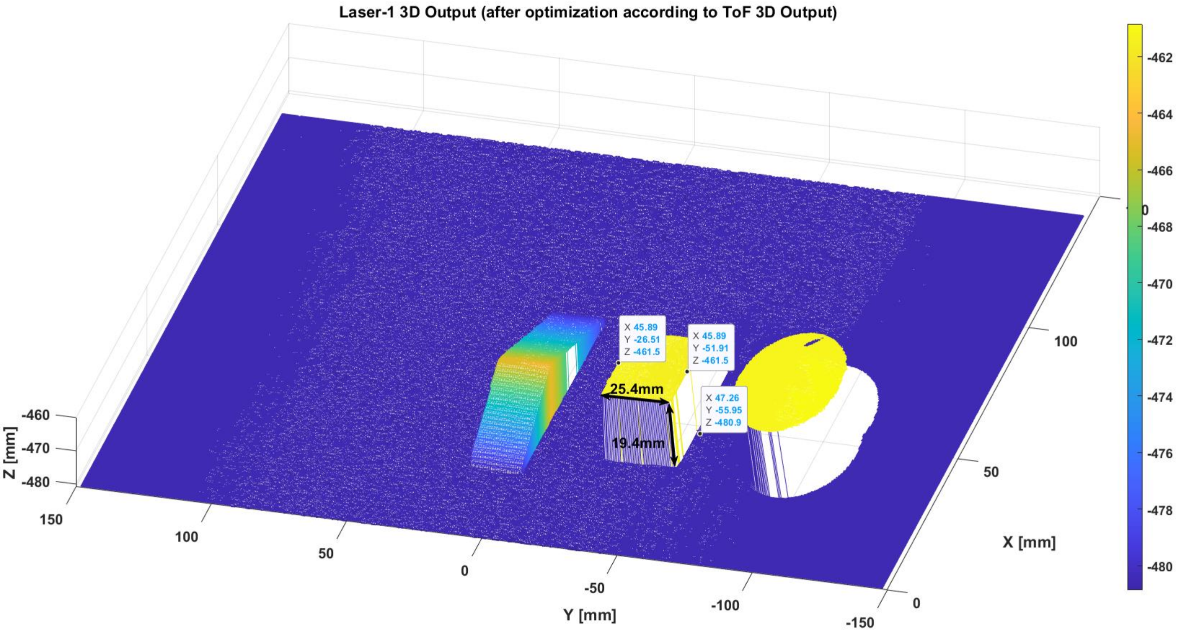

Figure 50. Laser-1 3D Output after Calibration according to ToF

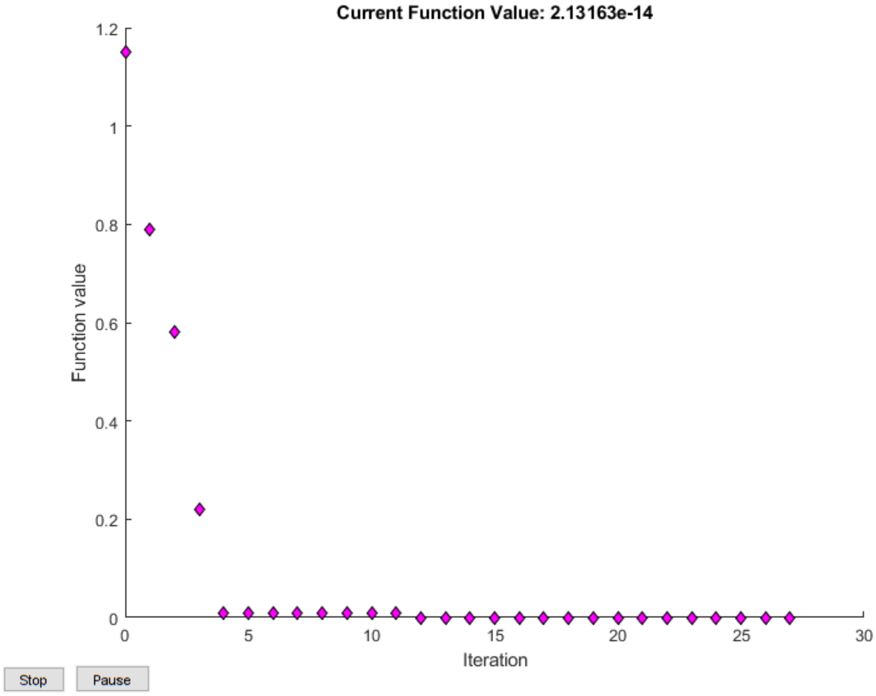

Figure 51. NMA Iteration for Laser 1 Calibration

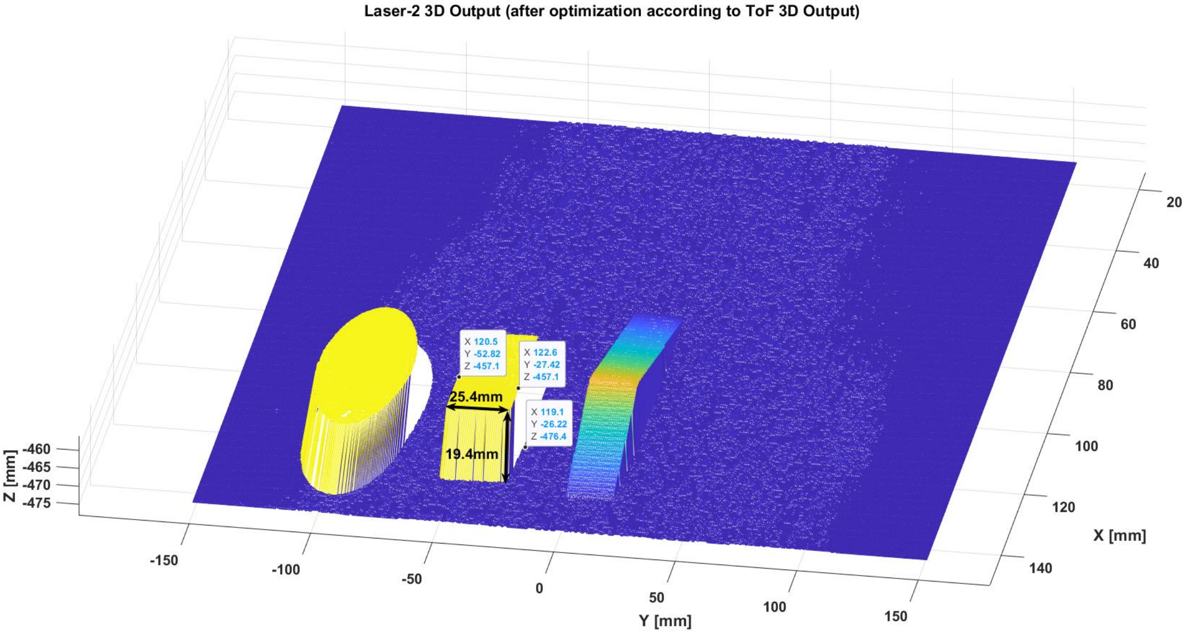

Figure 52. Laser-2 3D Output after Calibration according to ToF

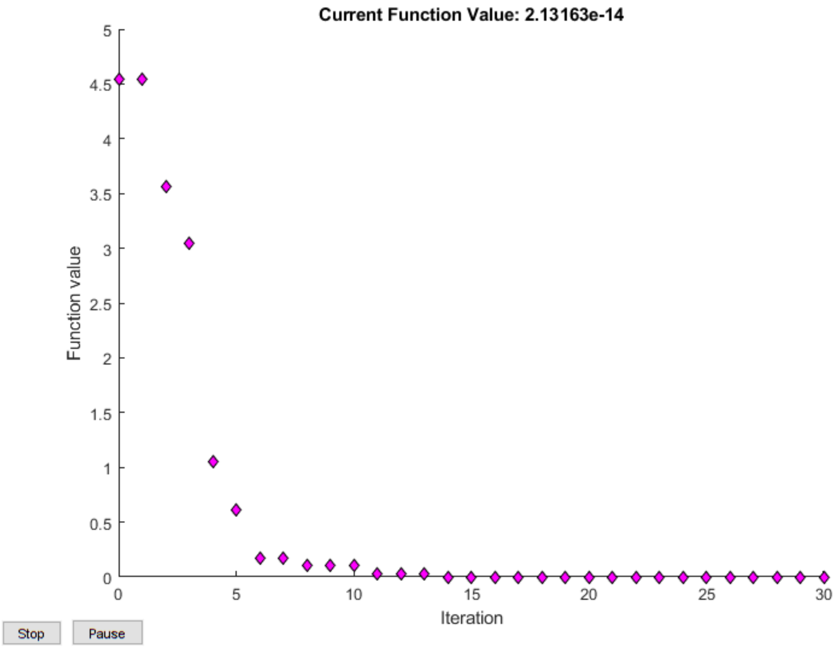

Figure 53. NMA Iteration for Laser 2 Calibration

4.2. Alignment of Laser Planes and ToF Plane

4.2.1. Elimination of Projection Path Occlusion with Two Laser Stripes

Due to the angular positions of laser stripes, projection path occlusion occurred in certain edges of objects. The laser stripe is not visible on some edges of the objects. As a result, these points have not been defined, and they should be empty in the 3D dataset. This situation is minimized by using two stripe lasers placed on different sides of the scanning surface. The region that one laser cannot observe is visible to the other laser. This is explained in detail in section 3.1.4.

The point clouds obtained from the two lasers were aligned and matched to the same points through optimization using the Nelder - Mead algorithm. In this optimization process, the objective function shown in equation 4.3 was utilized.

$$f\left(x_{\mathrm{laser}_1}\right) = \sum_{y=1}\left(\sum_{x=1}\left|Z_{\mathrm{laser}_{1_{xy}}} - Z_{\mathrm{laser}_{2_{xy}}}\right|\right) \tag{4.3}$$

According to this objective function, the differences in the z-values for the same x and y points of the two laser point clouds are minimized. The two lasers are attempting to decrease the value of z by moving along the x-axis in the point cloud. At the location where the differences in z-values are smallest, the two laser point clouds complement each other.

Figures 54 and 55 depict the occlusion regions caused by the angular positions of laser-1 and laser-2. As a result, when the 3D reconstruction structures obtained from the two lasers reconstruction are merged (Figures 56, 57) the projection path occlusion areas are eliminated. The opposing lasers complete their own occlusion regions. The final top-down view is shown in Figure 58. As depicted in Figure 58, the laser occlusion regions have disappeared, and only the camera occlusion region appears empty.

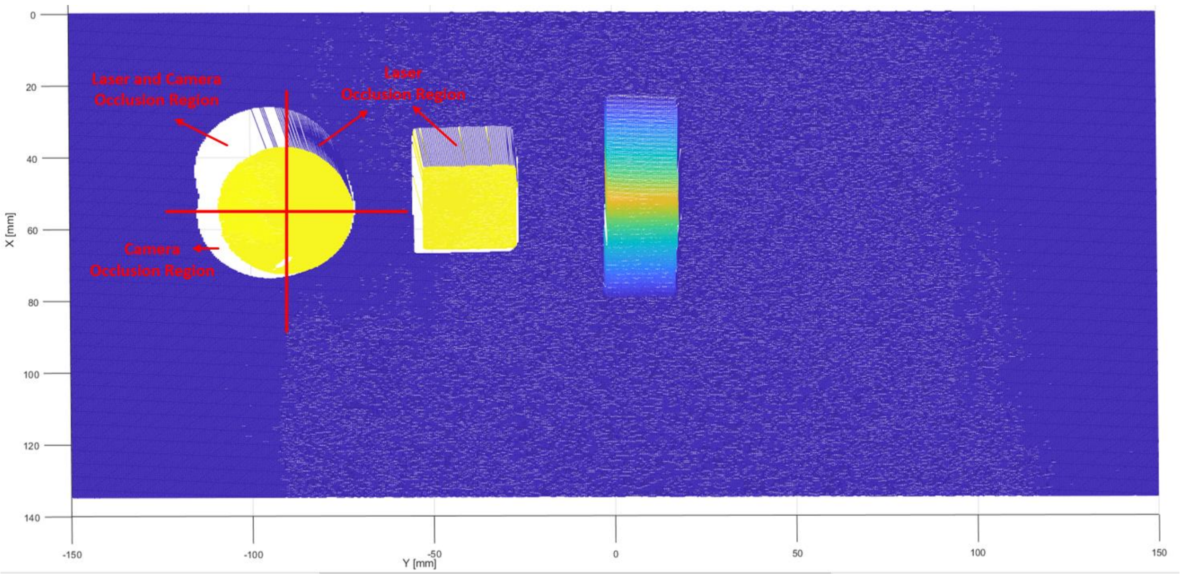

Figure 54. Laser-1 3D Reconstruction Top-View (Three objects)

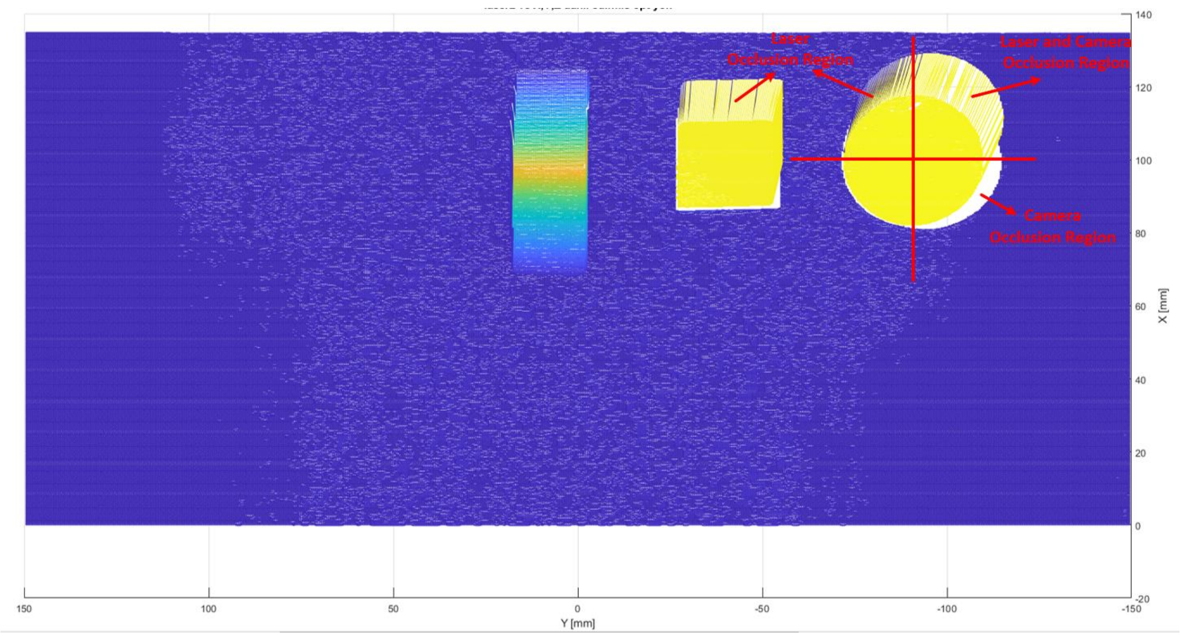

Figure 55. Laser-2 3D Reconstruction Top-View (Three objects)

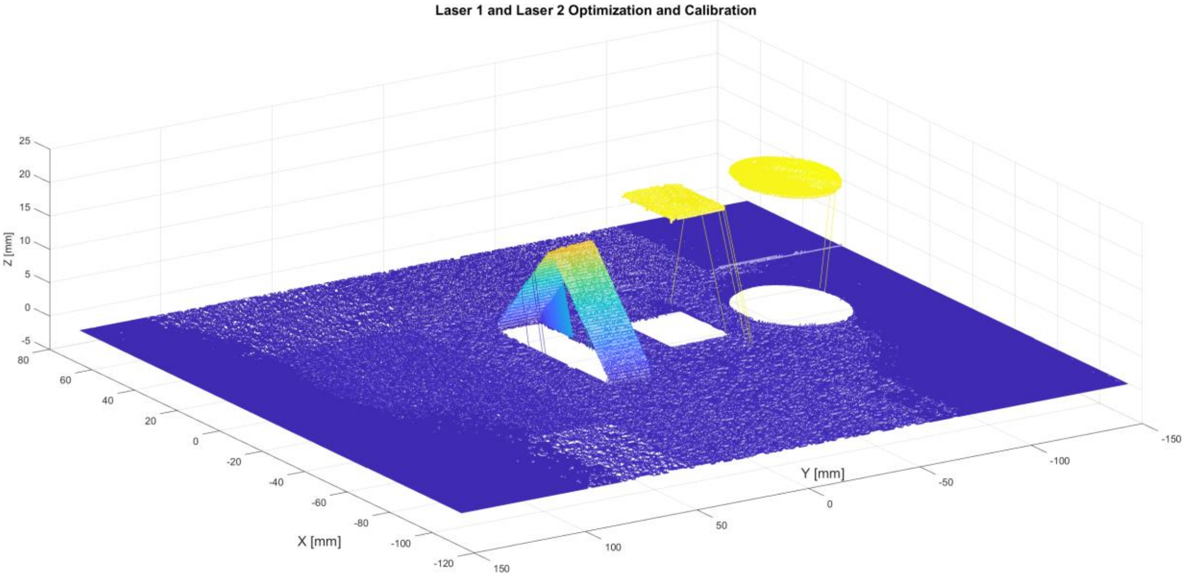

Figure 56. Cross View after laser 1 and laser 2 optimization (Three objects)

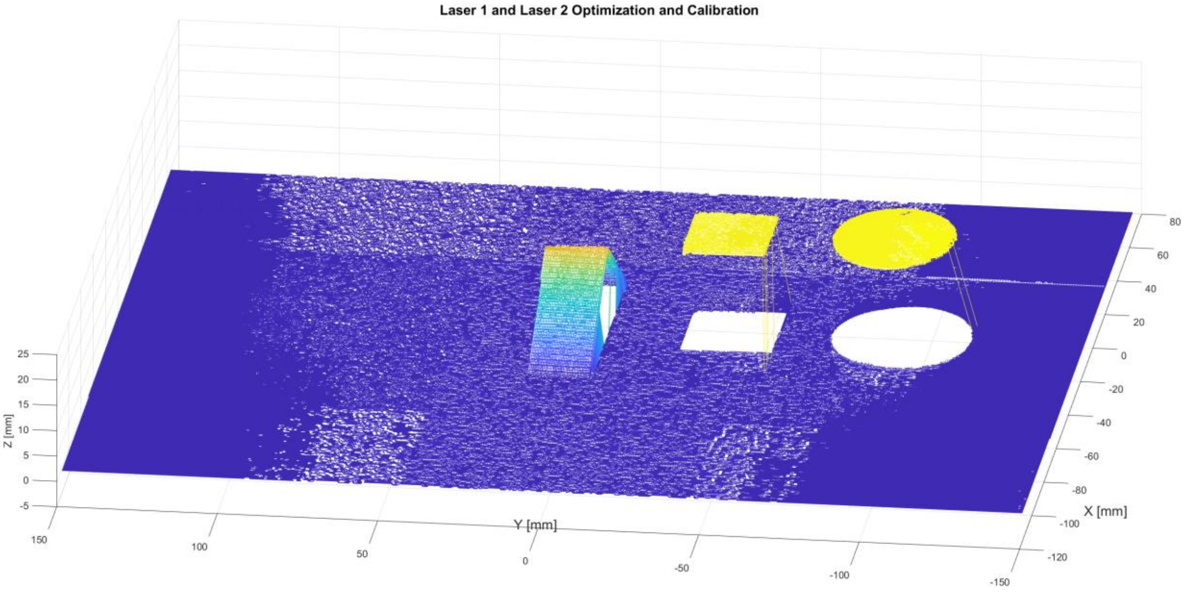

Figure 57. Front View after laser 1 and laser 2 optimization (Three objects)

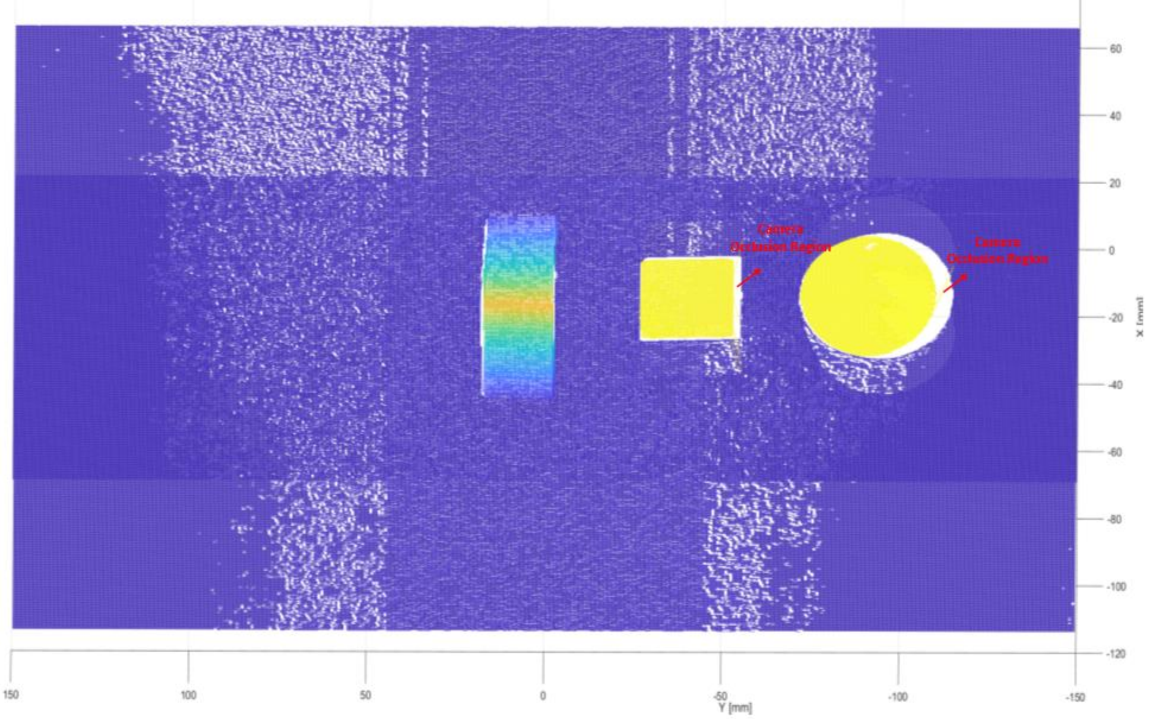

Figure 58. Top View laser 1 and laser 2 after optimization (Three objects)

In Figure 59, the optimization iteration graph of alignment for laser 1 and laser 2 is showed. According to the graph, the total sum of the differences in z-values for the same x and y points in the two lasers' coordinate system is 910. This value decreases with each iteration.

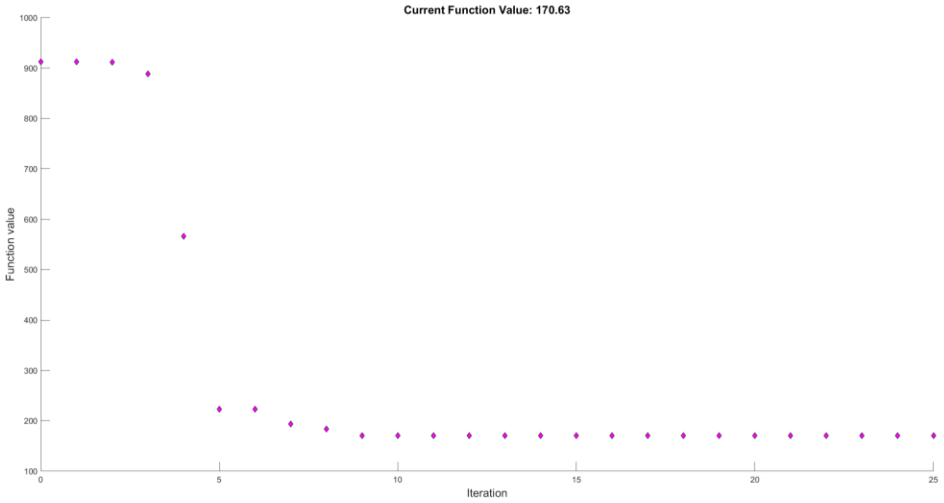

Figure 59. NMA Iteration for Laser 1 and Laser 2 Calibration

4.2.2. Elimination of Imaging Path Occlusion with Time of Flight Sensor

The Time of Flight (ToF) sensor can also be used to eliminate imaging path occlusion. It measures the time it takes for a light signal to travel from the sensor to the object and back, allowing for accurate distance measurements and depth sensing.

One of the advantages of ToF sensors is their ability to overcome occlusion issues. In traditional imaging systems, occlusion can occur when objects block the line of sight between the sensor and the target object (Ibaraki, et al., 2016). This can result in incomplete or inaccurate imaging data.

In this section, optimization was achieved by incorporating the ToF sensor point cloud, resulting in our final 3D reconstruction output. By minimizing error margins, this study ensures accurate results. Regions affected by camera occlusion were complemented using the ToF sensor output (Stankiewicz, et al., 2011). Figure 60 shows the output with only laser occlusion eliminated, while regions affected by camera occlusion are indicated. Figures 60, 61, and 62 demonstrate different perspective where the camera occlusion effect has been eliminated (Ye, et al., 2021).

After matching the planes using two laser optimizations, another optimization is performed by including the ToF sensor once again. The objective function is shown in equation 4.4. As a result of this process, the final 3D output is obtained.

$$\mathrm{f}(\mathrm{x}_{\mathrm{ToF}}) = \sum_{\mathrm{y}=1}\left(\sum_{\mathrm{x}=1}\left|\mathrm{Z}_{\mathrm{ToF}_{\mathrm{x,y}}} - \mathrm{Z}_{\mathrm{laser}_{1,2}{}_{\mathrm{x,y}}}\right|\right) \tag{4.4}$$

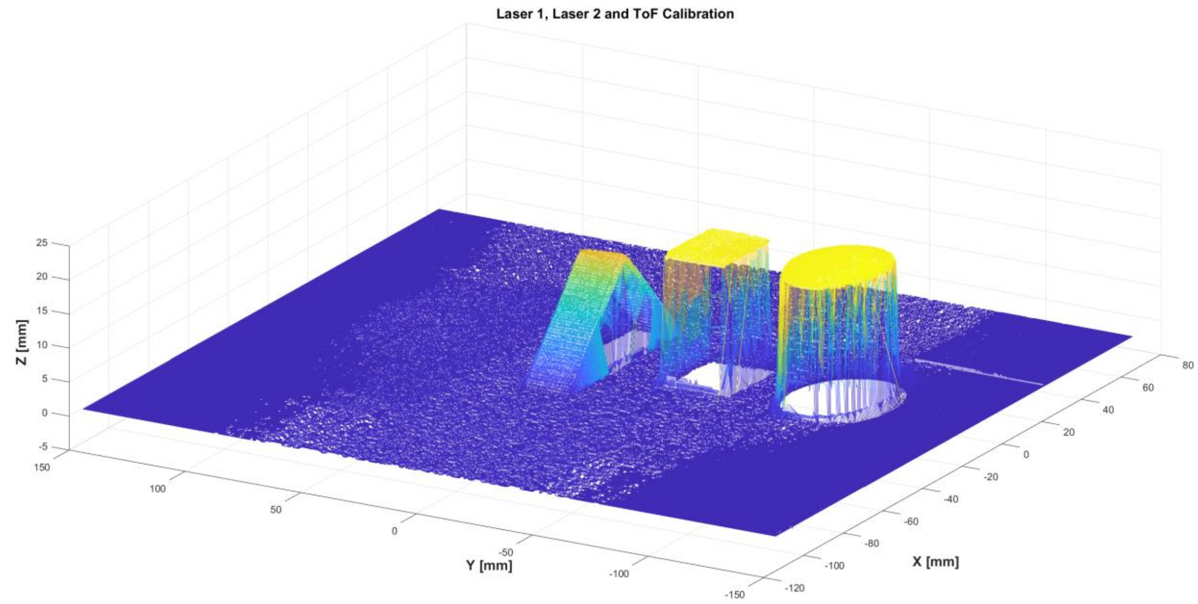

Figure 60. Cross View after optimization of laser 1, laser 2 and ToF (Three objects)

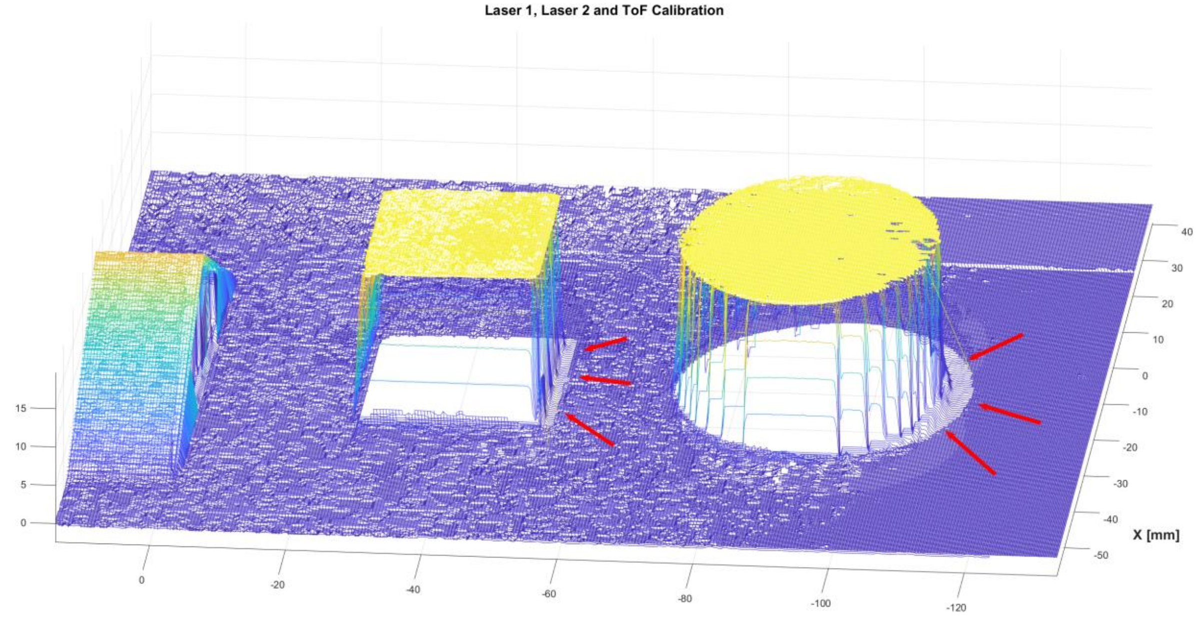

Figure 61. Front View after optimization of laser 1, laser 2 and ToF (Three objects)

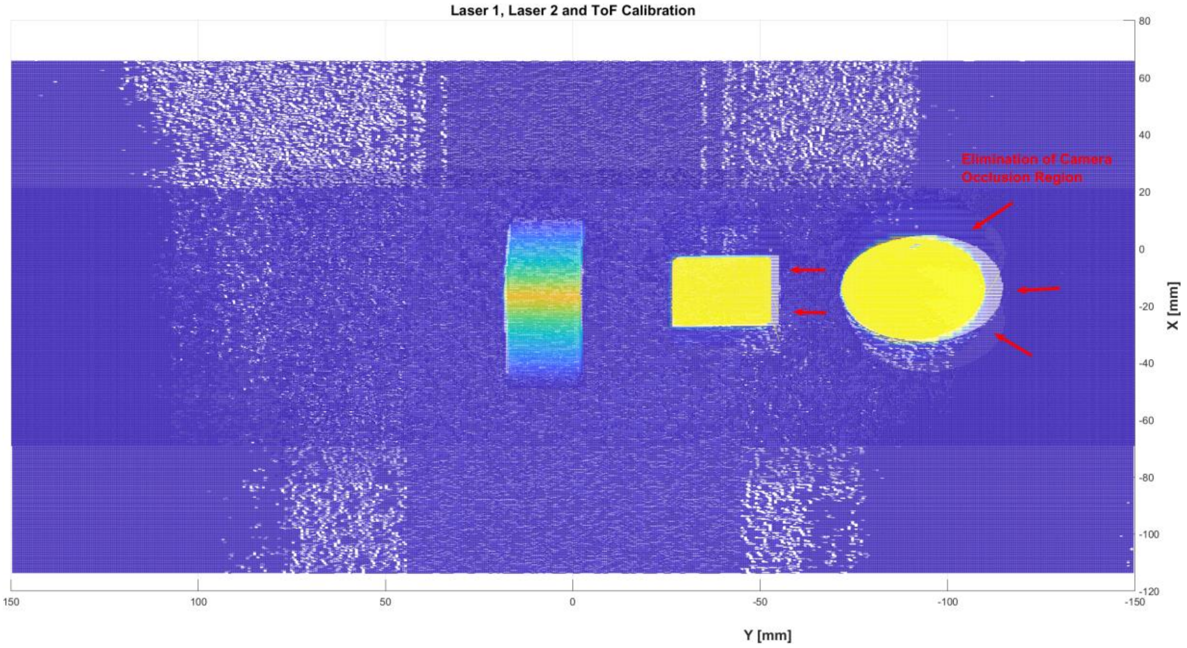

Figure 62. Top View after optimization of laser 1, laser 2 and ToF (Three objects)

The optimization process is completed after approximately 12-13 iterations, as shown in the NMA iteration graph below (Figure 63). The ToF sensor is aligned with laser1 and laser2 combination point cloud. As a result, Figure 62 illustrates the 3D reconstruction.

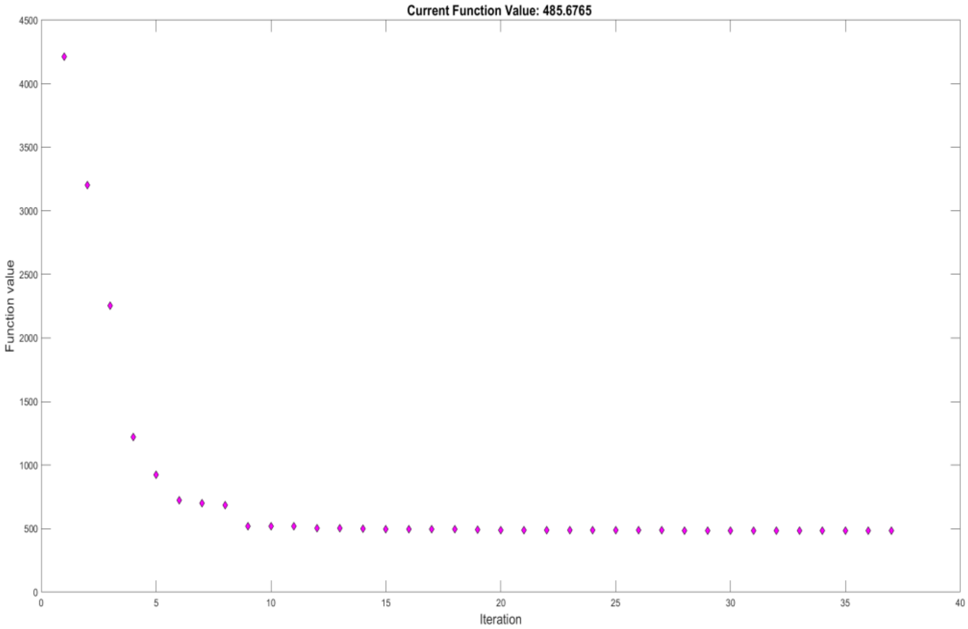

Figure 63. NMA Iteration for Laser 1, Laser 2 Combination and ToF Calibration

After completing the calibration process with three objects, results were demonstrated on different objects for testing purposes. As depicted in Figure 64, 65, five wooden pieces were randomly placed in the scanning area in different orientations or positions. Subsequently, laser and ToF scanning processes were carried out. Figure 66, 67 and 68 shows laser 1, laser 2, and ToF 3D output, respectively. By optimizing all the outputs, Figure 69 was obtained. As observed in Figure 69, a very good result was achieved. It can be seen that camera and laser occlusion areas have been eliminated in this result.

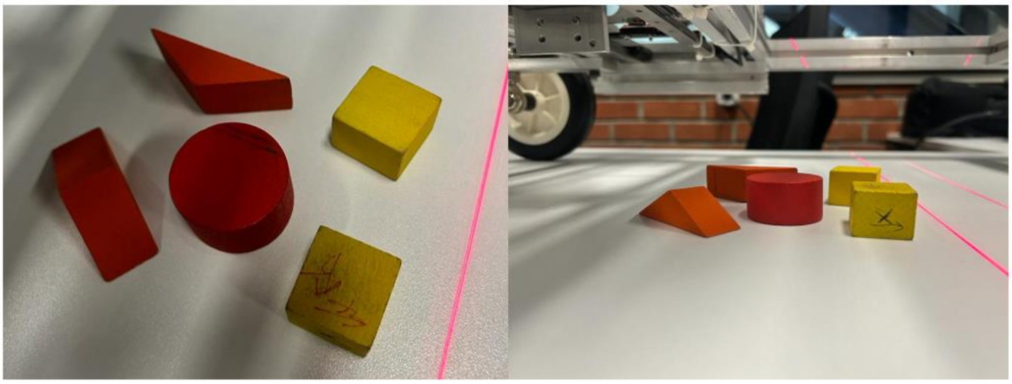

Figure 64. The positions of the five objects in Workspace

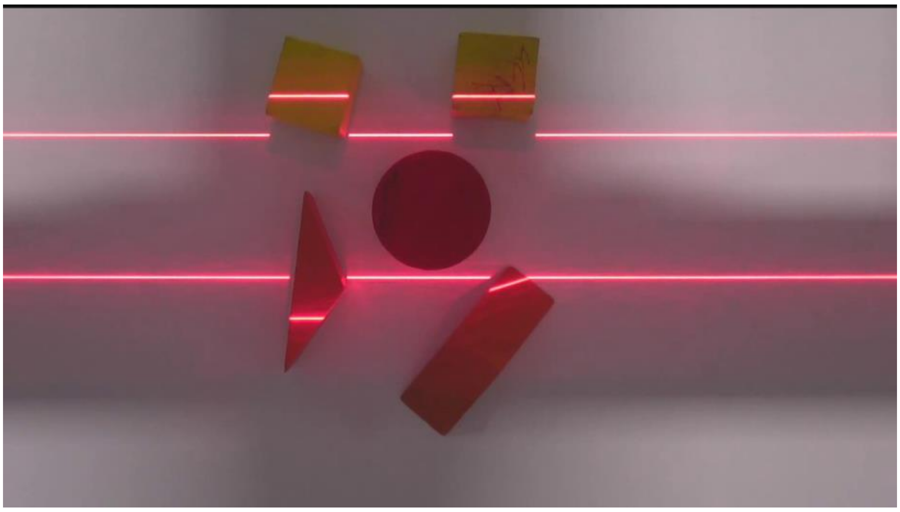

Figure 65. Camera Image during Scanning (Five Objects)

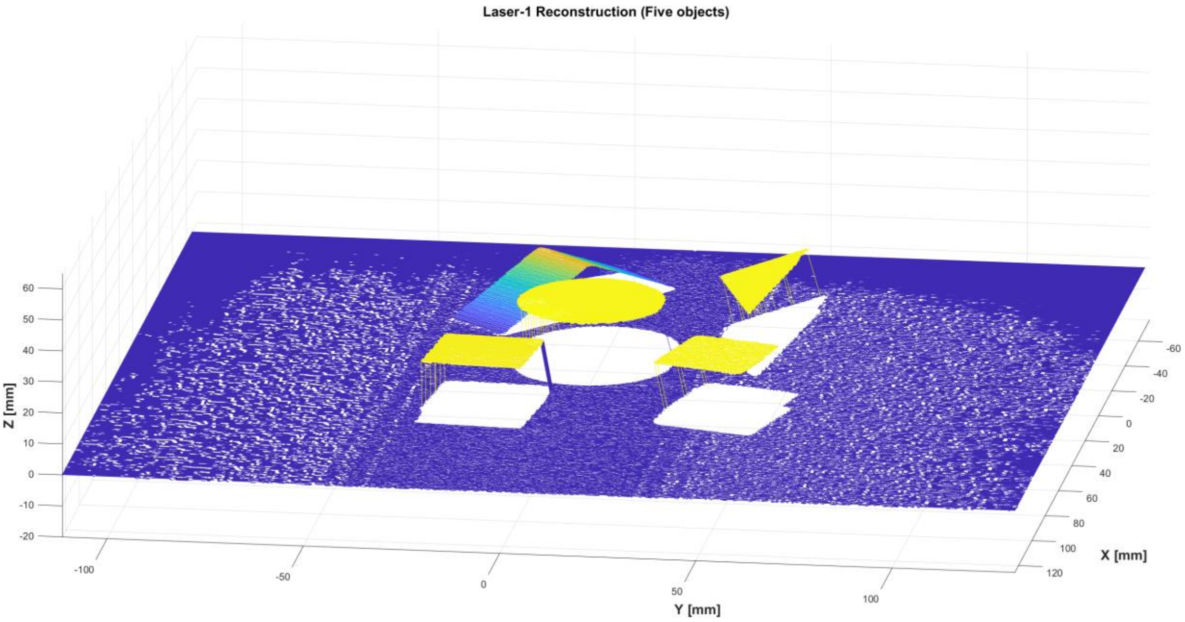

Figure 66. Laser-1 3D Reconstruction View (Five objects)

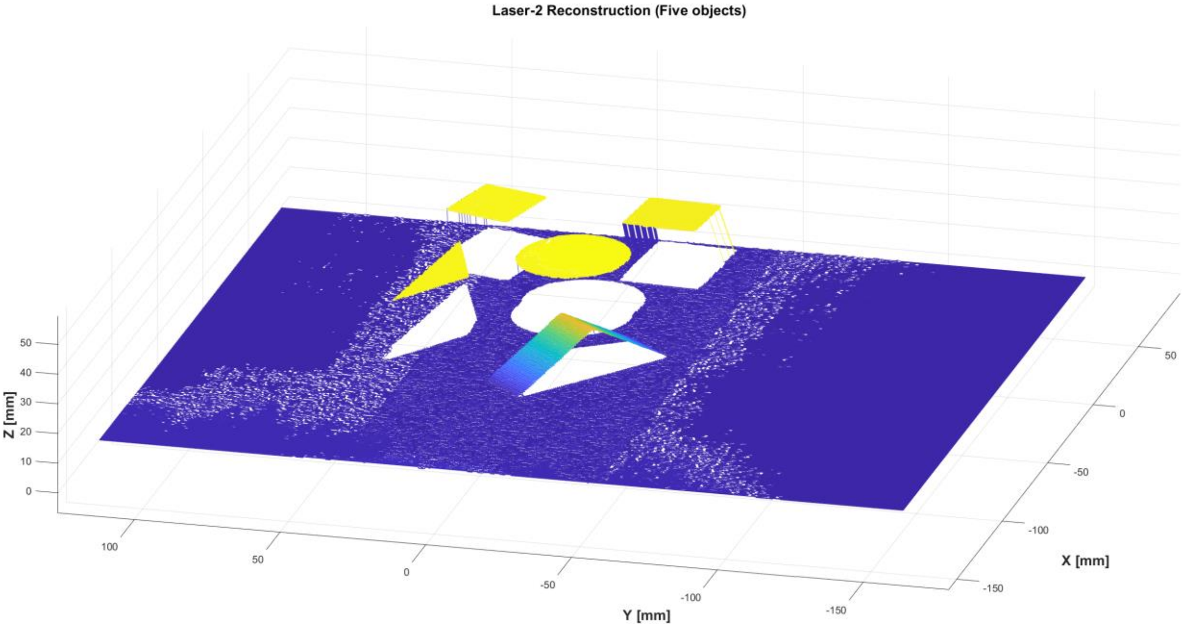

Figure 67. Laser-2 3D Reconstruction View (Five objects)

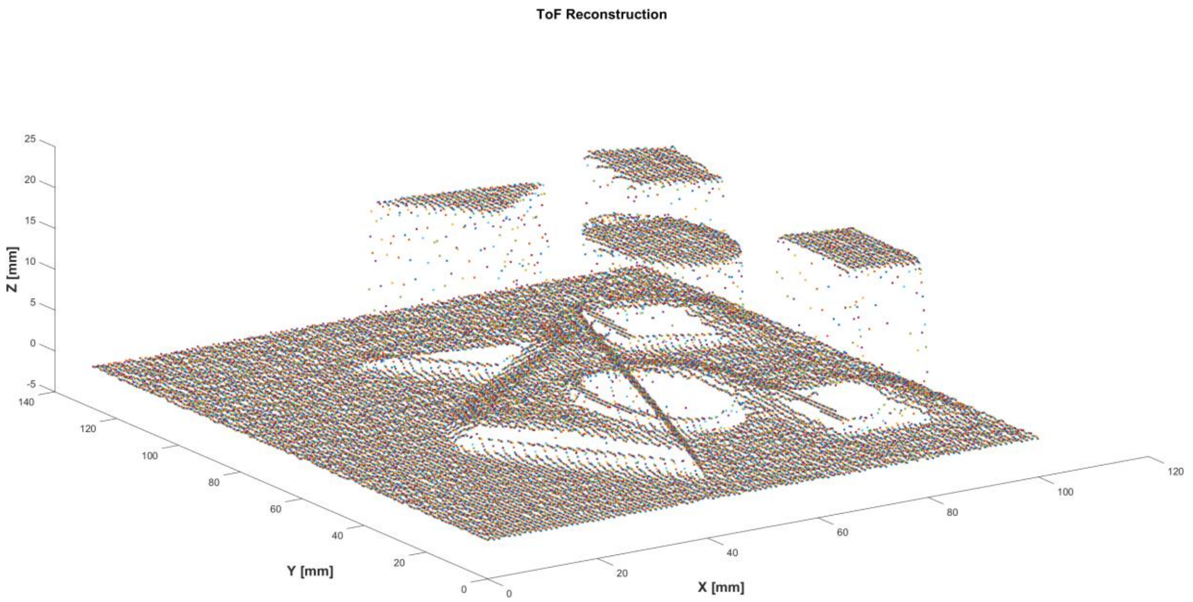

Figure 68. ToF 3D Output (Five objects)

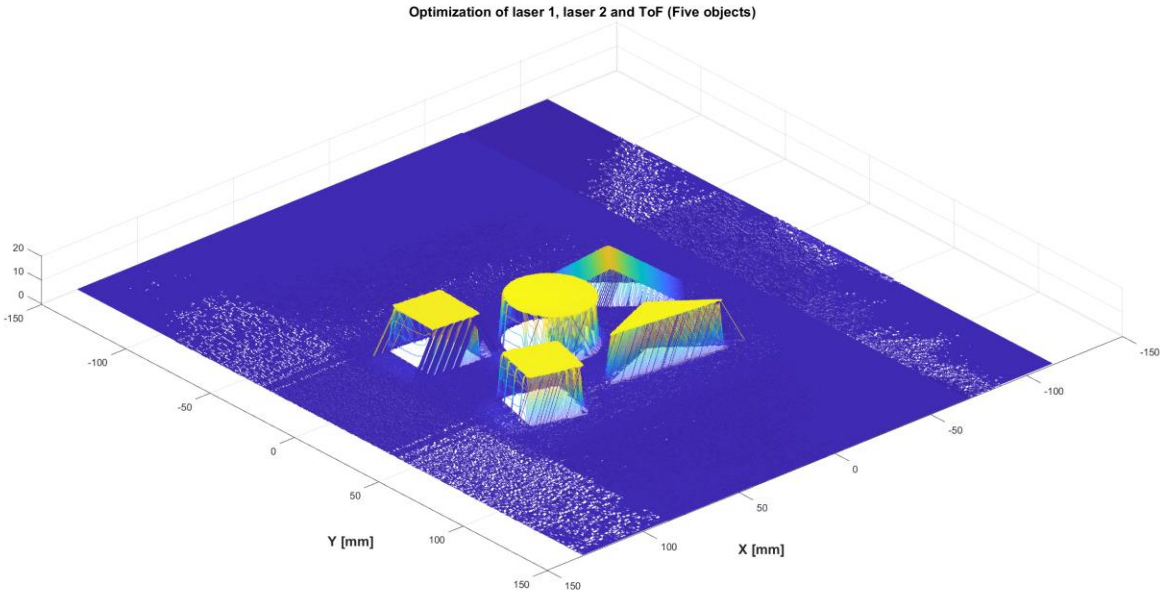

Figure 69. Cross View after optimization of laser 1, laser 2 and ToF (Five objects)

After using sharp-edged objects, the optimization results were examined with objects that have smoother contour transitions. For this study, the Pharaoh Silhouette object was selected. As seen in Figure 70, it has a complex shape with mixed forms.

Figure 70. Pharaoh Silhouette Object

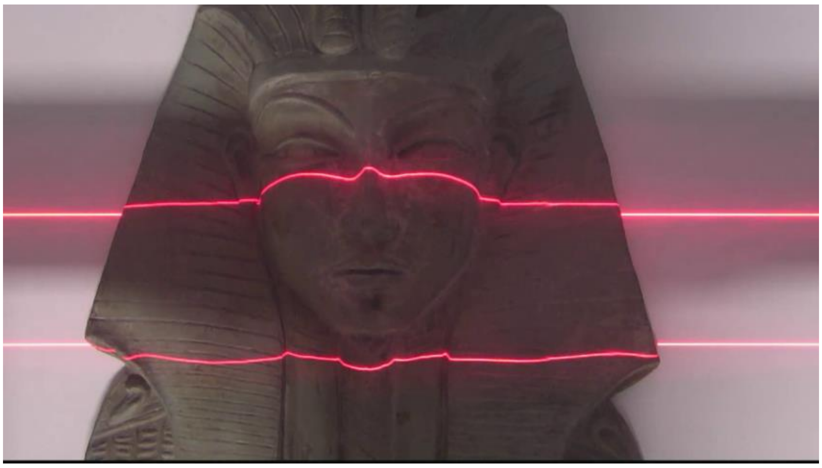

Figure 71. Camera Image during Scanning (Pharaoh Silhouette)

The top-view and cross-view images of the Pharaoh Silhouette object were presented in figures 72 and 73, respectively. The white areas remaining in the point cloud represent the camera and laser occlusion regions. It is anticipated that these white areas will disappear after the optimization process is conducted.

2.

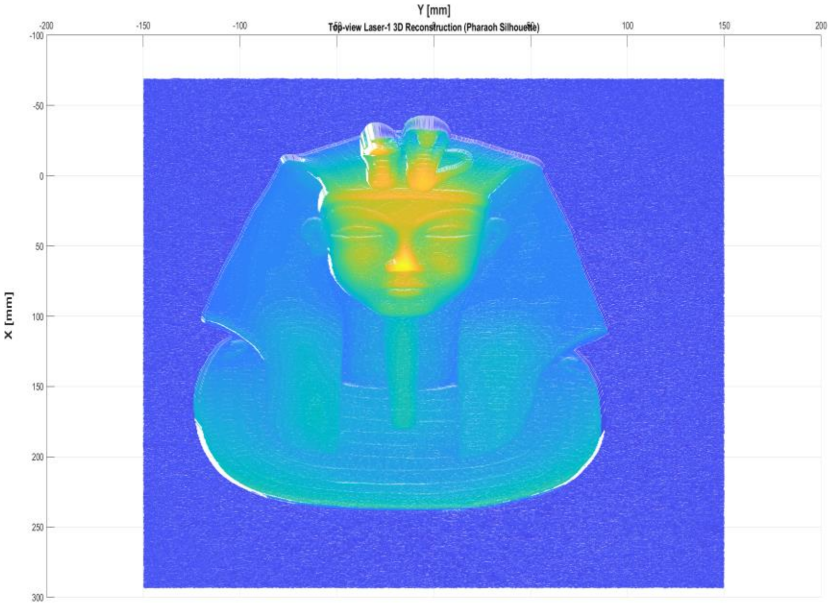

Figure 72. Top-view Laser-1 3D Reconstruction (Pharaoh Silhouette)

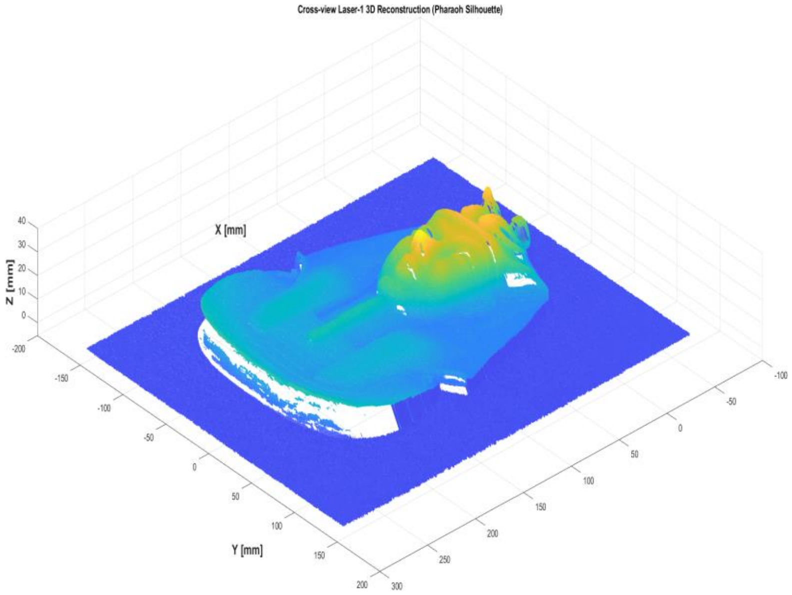

Figure 73. Cross-view Laser-1 3D Reconstruction (Pharaoh Silhouette)

Figure 74 and Figure 75 illustrate the 3D reconstruction process generated by laser 2.

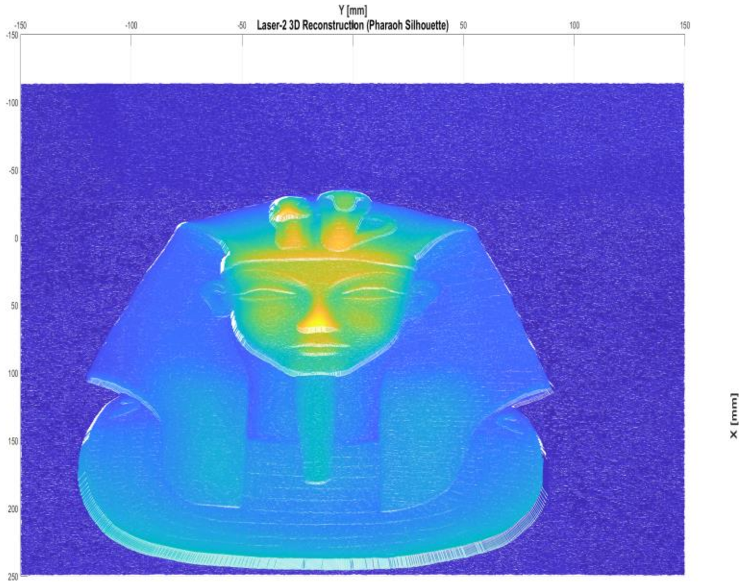

Figure 74. Top-view Laser-2 3D Reconstruction (Pharaoh Silhouette)

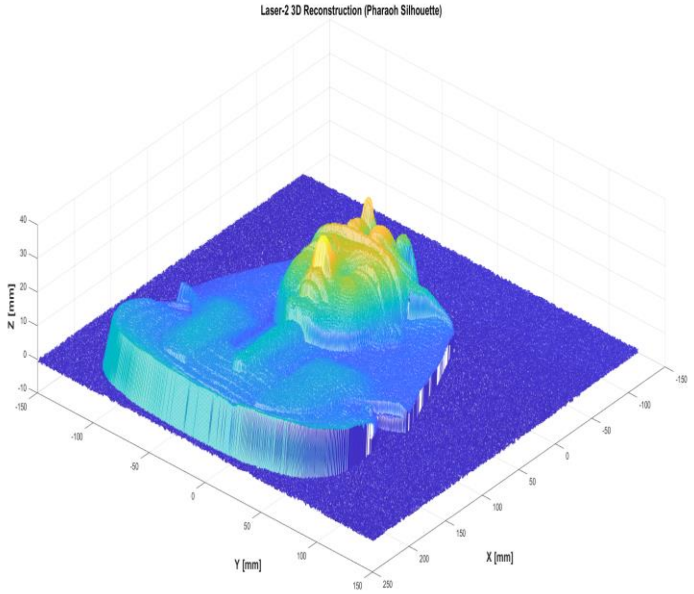

Figure 75. Cross-view Laser-2 3D Reconstruction (Pharaoh Silhouette)

Figure 76 shows the point clouds obtained from the ToF sensor. When the optimization process is applied to the point clouds from Laser 1 and Laser 2, Figure 69 and Figure 70 are obtained.

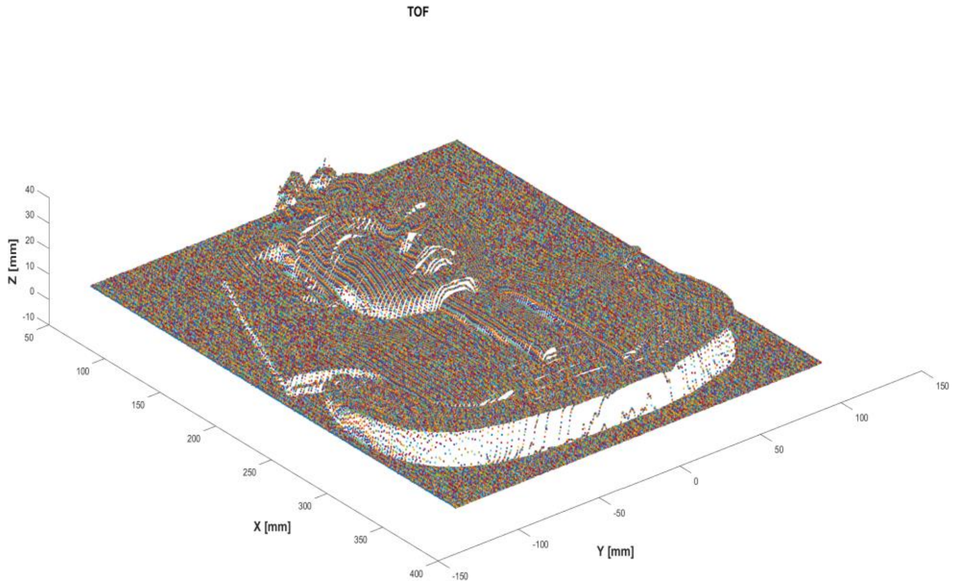

Figure 76. 3D Point Cloud of ToF (Pharaoh Silhouette)

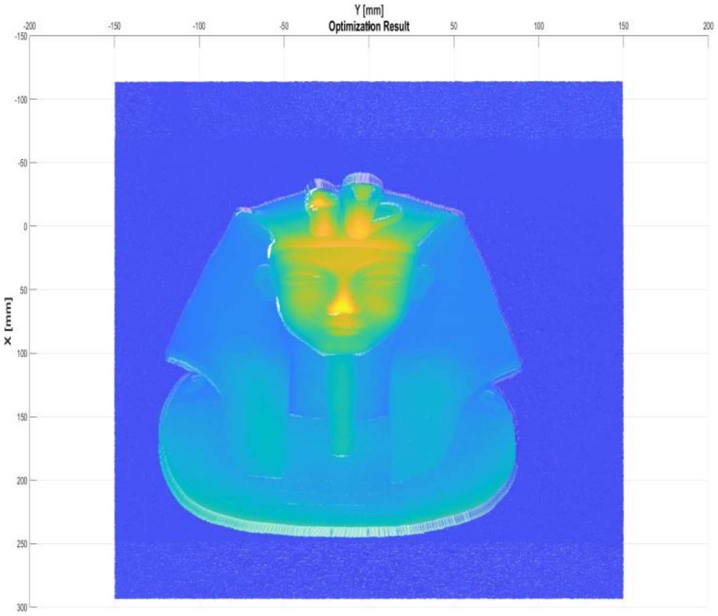

Figure 77. Top-view after optimization of Laser 1 and Laser 2 (Pharaoh Silhouette)

After the optimization process using Laser 1 and Laser 2, Figure 77 shows the presence of camera occlusion areas, as indicated by the red arrow. However, in Figure 79, the gaps visible in Figure 78 are not present. A complete form has been achieved.

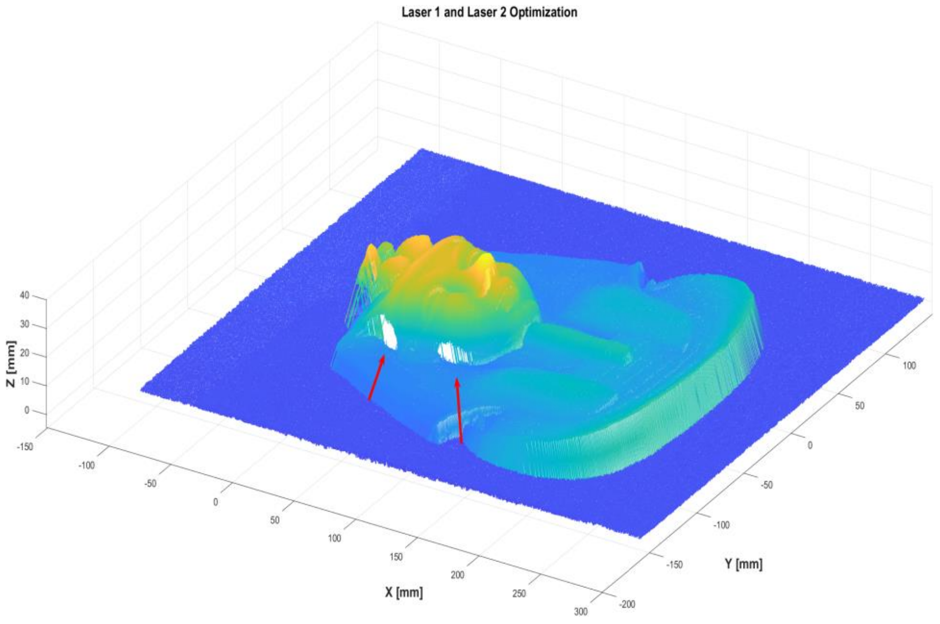

Figure 78. Cross-view after optimization of Laser 1 and Laser 2 (Pharaoh Silhouette)

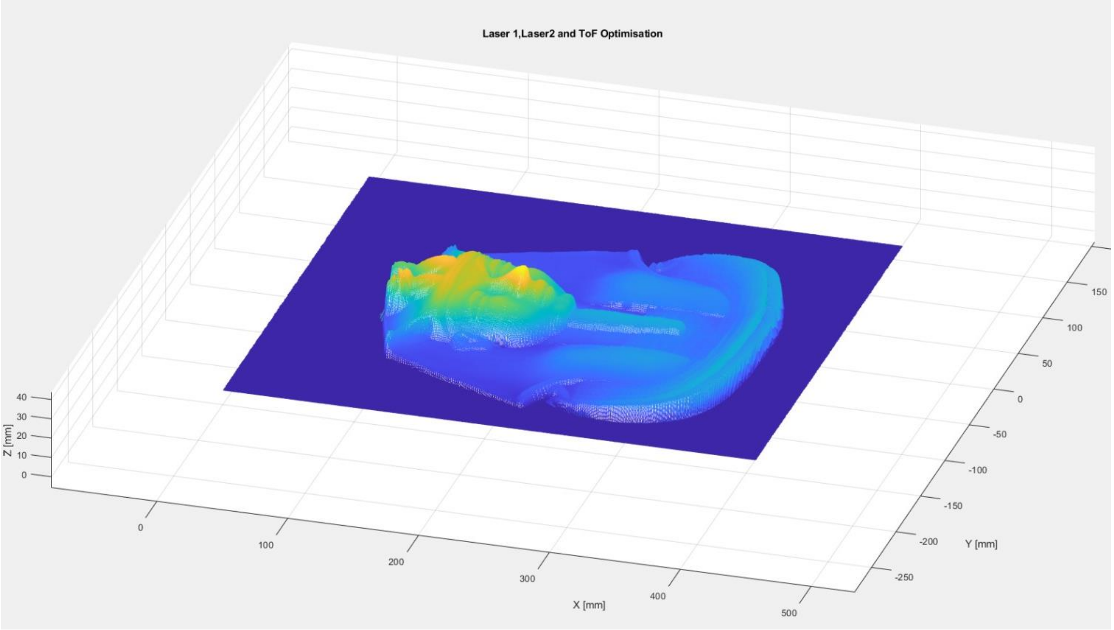

Figure 79. Cross-view after optimization of Lasers and ToF (Pharaoh Silhouette)

CHAPTER 5

CONCLUSIONS AND FUTURE WORKS

Our research and experiments have yielded several significant findings. Firstly, it has been proven that the integration of active triangulation, and flight time sensors is effective in obtaining accurate depth measurement and reducing occlusion problems during the scanning process. This integration has led to improved overall scanning performance and higher quality 3D model reconstructions.

The results obtained from our experiments have confirmed the effectiveness of the proposed system in accurately capturing complex geometry. This has made it a valuable tool for applications that require detailed 3D data. Moreover, the proposed system can achieve accurate results with minimal human interaction in real time.

Experimental results have demonstrated that the combined use of active triangulation and Time-of-Flight (ToF) sensor outperforms using lasers alone. Aligning the point clouds obtained from laser 1 and laser 2 resulted in more comprehensive and detailed 3D reconstructions with significantly reduced occlusion areas. The calibration process was further improved by optimizing the alignment between laser 1, laser 2, and the ToF sensor's point clouds to effectively eliminate camera occlusion areas.

Additionally, the system has showed its ability to process objects with different shapes and contours. The optimization process successfully reconstructed objects with sharp edges as well as those with smoother transitions, as demonstrated by sharp-edged objects and the Pharaoh Silhouette object.

However, there are still opportunities for further improvement and future research. Advanced algorithms and techniques for noise reduction and increasing the resolution of captured point clouds can enhance the overall quality of 3D reconstructions. Additionally, expanding the system's capabilities to process larger objects and improving quality of real-time performance would be valuable for practical applications. Integrating the scanning system with robotic systems or autonomous platforms could enable its use in various sectors such as manufacturing, inspection, and augmented reality.

To expand the applications of the system, integrating additional sensing methods such as capturing color or texture information would provide more comprehensive and visually appealing 3D models. This development can be utilized in fields such as computer graphics, where realistic and visually appealing models are required.

Furthermore, the system's portability and usability can be further enhanced to facilitate widespread adoption. Improving the system's ease of use would enable its deployment in various environments and industries, including architecture, archaeology, industrial design, and healthcare services.

In conclusion, the advanced real-time 3D scanning system utilizing the combined use of active triangulation and ToF sensors has shown promising results in capturing accurate and detailed 3D reconstructions. Further research and development efforts in calibration, noise reduction, real-time performance, and integration with other technologies can enhance the system's capabilities and expand its applications in various fields.

REFERENCES

Azevedo, Teresa C. S.. “3D object reconstruction using computer vision : reconstruction and characterization applications for external human anatomical structures.” (2012).

Bianco, Simone, Gianluigi Ciocca, and Davide Marelli. “Evaluating the Performance of Structure from Motion Pipelines.” Journal of Imaging 4, no. 8 (2018): 98. https://doi.org/10.3390/jimaging4080098.

Brandao, Pedro, “Autonomous Robot Control Using Night Vision Camera and TOF Sensor for Depth Scanning and Real-Time Object Recognition.” Solid State Technology, 2020

Chen, Xuzhan, Youping Chen, Bing Chen, Zhuo He, Yunxiu Ma, Dailin Zhang, and Homayoun Najjaran. “A Camera Intrinsic Matrix-Free Calibration Method for Laser Triangulation Sensor.” Sensors 21, no. 2 (2021): 559. https://doi.org/10.3390/s21020559.

Durante, Francesco, and Pierluigi Beomonte Zobel. “Development of a Time of Flight Laser Scanner 3D.” Advances in Intelligent Systems and Computing, 2017, 538–45. https://doi.org/10.1007/978-3-319-65960-2_66.

Eck, Ulrich, Michael Wechner, Frieder Pankratz, Kevin Yu, Marc Lazarovici, and Nassir Navab. “Real-Time 3D Reconstruction Pipeline for Room-Scale, Immersive, Medical Teleconsultation.” Applied Sciences 13, no. 18 (2023): 10199. https://doi.org/10.3390/app131810199.

Gao, Fuchang, and Lixing Han. “Implementing the Nelder-Mead Simplex Algorithm with Adaptive Parameters.” Computational Optimization and Applications 51, no. 1 (2010): 259–77. https://doi.org/10.1007/s10589-010-9329-3.

Gupta, Mohit, Amit Agrawal, Ashok Veeraraghavan, and Srinivasa G. Narasimhan. “Structured Light 3D Scanning in the Presence of Global Illumination.” CVPR 2011, 2011. https://doi.org/10.1109/cvpr.2011.5995321.

Ham, Hanry, Julian Wesley, and Hendra Hendra. “Computer Vision Based 3D Reconstruction : A Review.” International Journal of Electrical and Computer Engineering (IJECE) 9, no. 4 (2019): 2394. https://doi.org/10.11591/ijece.v9i4.pp2394-2402.

Ibaraki, Soichi, Yoshitomo Kitagawa, Yoshihiro Kimura, and Shizuo Nishikawa. “On the Limitation of Dual-View Triangulation in Reducing the Measurement Error Induced by the Speckle Noise in Scanning Operations.” The International Journal of Advanced Manufacturing Technology 88, no.1–4 (2016): 731–37. https://doi.org/10.1007/s00170-016-8787-x.

Jens Guehring "Dense 3D surface acquisition by structured light using off-the-shelf components", Proc. SPIE 4309, Videometrics and Optical Methods for 3D Shape Measurement, (22-December 2000); https://doi.org/10.1117/12.410877

Jung, Jiyoung, Joon-Young Lee, Yekeun Jeong, and In So Kweon. “Time-of-Flight Sensor Calibration for a Color and Depth Camera Pair.” IEEE Transactions on Pattern Analysis and Machine Intelligence 37, no. 7 (2015): 1501–13. https://doi.org/10.1109/tpami.2014.2363827.

Lindner, Marvin, Ingo Schiller, Andreas Kolb, and Reinhard Koch. “Time-of-Flight Sensor Calibration for Accurate Range Sensing.” Computer Vision and Image Understanding 114, no. 12 (2010): 1318–28. https://doi.org/10.1016/j.cviu.2009.11.002.

Moncef, Aharchi, and M’hamed Aït Kbir. “Overview on 3D Reconstruction from Images.”Proceedings of the 4th International Conference on Smart City Applications, 2019. https://doi.org/10.1145/3368756.3369106.

Munaro, Matteo, Edmond Wai So, Stefano Tonello, and Emanuele Menegatti. "Efficient Completeness Inspection Using Real-Time 3D Color Reconstruction with a Dual-Laser Triangulation System." Integrated Imaging and Vision Techniques for Industrial Inspection, 2015, 201–25. https://doi.org/10.1007/978-1-4471-6741-9_7.

Nguyen, Hoa G., and Michael R. Blackburn. A simple method for range finding via laser triangulation. 1995. https://doi.org/10.21236/ada292529.

Ntouskos, Valsamis & Kalisperakis, Ilias & Karras, George. "Automatic calibration of digital cameras using planar chess-board patterns." Optical 3-D Measurement Techniques VIII. 2007.

Nucleo-F746ZG. Mbed. Accessed September 15, 2023. https://os.mbed.com/platforms/ST-Nucleo-F746ZG/.

Ozan, and Gümüştekin. "Calibration of Double Stripe 3D Laser Scanner Systems Using Planarity and Orthogonality Constraints." Digital Signal Processing 24 (2014): 231–43. https://doi.org/10.1016/j.dsp.2013.08.006.

Ozan, Sukru, and Sevket Gumustekin. "Calibration of a 3D Environmet Scanner with a Pairof Line Lasers." 2012 20th Signal Processing and Communications Applications Conference (SIU), 2012. https://doi.org/10.1109/siu.2012.6204468.

Peiravi, Ali & Taabbodi, Behrai. "A Reliable 3D Laser Triangulation-based Scanner with a New Simple but Accurate Procedure for Finding Scanner Parameters. "Marsland Press Journal of American Science, 2007.

Pulcrano, M., S. Scandurra, G. Minin, and A. di Luggo. “3D Cameras Acquisitions for the Documentation of Cultural Heritage.” The International Archives of the Photogrammetry, Remote Sensing and Spatial Information Sciences XLII-2/W9 (2019): 639–46. https://doi.org/10.5194/isprs-archives-xlii-2-w9-639-2019.

Rodríguez-Martín, Manuel, and Pablo Rodríguez-Gonzálvez. “Suitability of Automatic Photogrammetric Reconstruction Configurations for Small Archaeological Remains.”Sensors 20, no. 10 (2020): 2936. https://doi.org/10.3390/s20102936.

So, Edmond Wai, Stefano Michieletto, and Emanuele Menegatti. “Calibration of a Dual-Laser Triangulation System for Assembly Line Completeness Inspection.” 2012 IEEE International Symposium on Robotic and Sensors Environments Proceedings, 2012. https://doi.org/10.1109/rose.2012.6402621.

Stankiewicz, M., J. Reiner, and G. Kotnarowski. “Positioning of Scanned Part inside of the Laser Triangulation System.” SPIE Proceedings, 2011. https://doi.org/10.1117/12.889469.

Stepper Motor. AccessScience, n.d. https://doi.org/10.1036/1097-8542.654800.

Ye, Guoyong, Yuhao Zhang, Wei Jiang, Siren Liu, Lei Qiu, Xiaojun Fan, Hongwen Xing, Pingping Wei, Bingheng Lu, and Hongzhong Liu. “Improving Measurement Accuracy of Laser Triangulation Sensor via Integrating a Diffraction Grating. ” Optics and Lasers in Engineering 143 (2021): 106631. https://doi.org/10.1016/j.optlaseng.2021.106631.

Žbontar, Klemen, Matjaž Mihelj, Boštjan Podobnik, Franc Povše, and Marko Munih. “Dynamic Symmetrical Pattern Projection Based Laser Triangulation Sensor for Precise Surface Position Measurement of Various Material Types.” Applied Optics 52, no. 12 (2013): 2750. https://doi.org/10.1364/ao.52.002750.

Zheng, Ling, Bijun Li, Bo Yang, Huashan Song, and Zhi Lu. “Lane-Level Road Network Generation Techniques for Lane-Level Maps of Autonomous Vehicles: A Survey.”Sustainability 11, no.16 (2019): 4511. https://doi.org/10.3390/su11164511.